# Human anti-smallpox long-lived memory B cells are defined by dynamic interactions in the splenic niche and long-lasting germinal center imprinting

Pascal Chappert, François Huetz, Marie-Alix Espinasse, Fabrice Chatonnet, Louise Pannetier, Lucie da Silva, Clara Goetz, Jérome Mégret, Aurélien Sokal, Etienne Crickx, et al.

# Human anti-Smallpox long-lived memory B cells are defined by dynamic interactions in the splenic niche and long-lasting germinal center imprinting

Pascal Chappert*[1,2,3], François Huetz*[1,4], Marie-Alix Espinasse*[1], Fabrice Chatonnet[5,6], Louise Pannetier**[1], Lucie Da Silva**[1], Clara Goetz[1], Jérôme Megret[7], Aurélien Sokal[1], Etienne Crickx[1,8], Ivan Nemazanyy[7], Vincent Jung[7], Chiara Guerrera[7], Sébastien Storck[1], Matthieu Mahévas[1,3,8], Antonio Cosma[9], Patrick Revy[10], Thierry Fest[5,6], Claude-Agnès Reynaud†[1], Jean-Claude Weill†[1].

* these authors contributed equally.

** these authors contributed equally.

† shared senior authorship

1. Institut Necker Enfants Malades (INEM), INSERM U1151/CNRS UMR 8253, Université Paris Cité, Paris, France.

2. Inovarion, Paris, France.

3. Institut Mondor de Recherche Biomédicale (IMRB), INSERM U955, équipe 2. Université Paris-Est Créteil (UPEC), Créteil, France.

4. Institut Pasteur, Université Paris Cité, Unité Anticorps en thérapie et pathologie, UMR 1222 INSERM, France.

5. Université de Rennes 1, INSERM, Établissement Français du Sang de Bretagne, UMR_S1236, Rennes, France.

6. Laboratoire d'Hématologie, Pôle de Biologie, Centre Hospitalier Universitaire, Rennes, France.

7. Structure Fédérative de Recherche Necker, INSERM US24-CNRS UAR3633, Paris, France.

8. Service de Médecine Interne, Centre Hospitalier Universitaire Henri-Mondor, Assistance Publique-Hôpitaux de Paris (AP-HP), Université Paris-Est Créteil (UPEC), Créteil, France.

9. Translational Medicine Operations Hub, National Cytometry Platform, Luxembourg Institute of Health, Esch-sur-Alzette, Luxembourg.

10. INSERM UMR 1163, Laboratory of Genome Dynamics in the Immune System, labellisé Ligue Nationale contre le Cancer, Imagine Institute, Université Paris Cité, Paris, France.

To whom correspondence should be addressed: pascal.chappert@inserm.fr, jean-claude.weill@inserm.fr or claude-agnes.reynaud@inserm.fr.

Lead Contact: Pascal Chappert (pascal.chappert@inserm.fr).

**Summary**

Memory B cells (MBCs) can persist for a lifetime, but the mechanisms that allow their long-term survival remain poorly understood. Here, we isolated and analyzed human splenic Smallpox/Vaccinia protein B5-specific MBCs in individuals who were vaccinated more than forty years ago. Only a handful of clones persisted over such an extended period and they displayed limited intra-clonal diversity with signs of extensive affinity-based selection. These long-lived MBCs appeared enriched in a $CD21^{hi}CD20^{hi}$ $IgG^{+}$ splenic B cell subset displaying a marginal zone-like NOTCH/MYC-driven signature but they did not harbor a unique longevity-associated transcriptional or metabolic profile. Finally, the telomeres of B5-specific long-lived MBCs were longer than those in patient-paired naive B cells in all samples analyzed. Overall, these results imply that separate mechanisms such as early telomere elongation, affinity selection during the contraction phase and access to a specific niche contribute to ensuring the functional longevity of MBCs.

## Introduction

Immune memory is usually defined as the ability to respond faster and more potently to a re-exposure to the same or closely related pathogen, a key attribute of the adaptive T and B cell components of the immune system. The humoral arm of immune memory is composed of memory B cells (MBCs) and long-lived plasma cells (PCs), which emerge during T dependent germinal center (GC) responses in which stringent antigen driven selection takes place (Victora and Nussenzweig, 2012). In humans, MBCs are detected several decades after infection or vaccination (Amanna, 2007; Crotty et al., 2003; Yu et al., 2008) and can provide rapid protection even in the total absence of PCs and neutralizing antibodies (Bauer and Jilg, 2006).

Most studies on the fate of B cell memory have been performed using different fate-mapping mouse models. The current paradigm coming from these studies is that MBCs leave the GC at an earlier time point than PCs and display an overall lower affinity for the immunizing antigen (Viant et al., 2020, 2021; Weisel et al., 2016; Wong et al., 2020), this property allowing them to respond to variants of the initial pathogen. $IgG^+$ B cells tend to dominate the GC reaction and display higher mutation loads (Pape et al., 2011; Sundling et al., 2021). However, both $IgM^+$ and $IgG^+$ MBCs have been observed to be stable for more than a year (Jones et al., 2015; Pape et al., 2018).

Studies tracking the generation of human MBCs following vaccination (Andrews et al., 2019; Goel et al., 2021; Kim et al., 2022; Matsuda et al., 2019; Wec et al., 2020) or natural infection (Davis et al., 2019; Gaebler et al., 2021; Sokal et al., 2021a, 2021b; Wang et al., 2021) have shown a sustained GC output of MBCs up to six months after challenge, these cells reaching maximal mutational load after that time point in most cases. Mid to high affinity antigen-specific MBCs could be tracked in the blood for over a year with evidence of a contraction phase before that time point in some (Andrews et al., 2019; Davis et al., 2019; Wec et al., 2020) but not all reports (Matsuda et al., 2019; Sokal et al., 2021b; Wang et al., 2021).

Recent deep single cell analyses have further highlighted the heterogeneity of human MBCs, both between and inside major lymphoid organs, through markers like Tbet and CD11c for effector/memory B cells, FCRL5 in tonsils and CD69, CD73 or CD45RB in the spleen and gut-associated lymphoid tissues (Glass et al., 2020; Johnson et al., 2020; King

et al., 2021; Sanz et al., 2019; Weisel et al., 2020, 2022; Zhao et al., 2018). Whether one of these subpopulations represents a unique long-lived MBC subset and whether a specific niche exists for these cells, alike long-lived PCs in the bone marrow (Nguyen et al., 2021), is still largely unknown.

Assessing the true longevity of human MBCs against common pathogens is, in most settings, hindered by the possibility for any given individual to re-encounter them during his lifetime. Smallpox, officially declared eradicated in 1980 (Fenner et al., 1988), represents one notable exception. Alongside smallpox eradication, anti-smallpox vaccination, based on the live Vaccinia virus, was progressively discontinued during the 1970s. Any detectable anti-Vaccinia memory B cell in an individual post 2010 would thus likely have been generated more than 40 years ago, without any re-stimulation with the immunizing antigen during that timeframe. Anti-Vaccinia antibodies serum titers remain stable in human for more than 80 years after first vaccination (Amanna, 2007; Hammarlund et al., 2003; Taub et al., 2008), with several identified immunodominant epitopes. This includes the glycoprotein B5, one of the five proteins from the extracellular enveloped virion (EEV) form of Vaccinia and known target of potent neutralizing antibodies (Aldaz-Carroll et al., 2005; Gilchuk et al., 2016; Lantto et al., 2011). Anti-Vaccinia MBCs have similarly been followed longitudinally in the blood for up to 65 years post vaccination (Amanna, 2007; Crotty et al., 2003). Following a contraction phase taking place in the first couple of years after immunization, they reach a remarkably stable plateau that last for decades at around 0.1% of total circulating $IgG^+$ MBCs. Functional analysis of such long-lived MBCs, however, is still lacking.

We reported previously that the spleen was enriched for these long-lived Vaccinia-specific MBCs (Mamani-Matsuda et al., 2008). We describe here the isolation and functional study of human splenic anti-Vaccinia MBCs, more than 40 years after vaccination. This enabled us to decipher the diversity and affinity of their repertoire as well as their transcriptional signature as compared to other splenic MBC populations. Our results suggest an extended contraction phase, driven by affinity selection, and elongated telomeres acquired in GCs, together with signals provided by a specific splenic niche, as the molecular basis for the functional longevity of these cells.

## Results

### Long-lived splenic Vaccinia-specific MBCs reside in the splenic CD73$^+$CD21$^+$CD27$^+$ IgG$^+$ B cell population.

As a proxy to study long-lived MBCs, we elected to isolate Vaccinia glycoprotein B5-specific cells from organ donors pre-enriched IgG$^+$ splenic MBCs (**Figure 1A and S1A**). B5-stained cells represented between 0.003 and 0.07% of total IgG$^+$ MBCs in the spleen of most organ donors born before 1970 and likely vaccinated during their childhood **(Figure 1A)**. These frequencies are in line with the previously estimated pool of long-lived MBCs against all Vaccinia antigens ranging between 0.02 and 0.3% of MBCs in the blood of most vaccinated donors and up to 0.6% in the spleen (Crotty et al., 2003; Mamani-Matsuda et al., 2008).

Starting from frozen vials of 30-60x10$^6$ splenocytes, this usually allowed us to sort between 20 to 200 cells of interest, with only a handful of donors above 100 cells. These extremely low frequencies and numbers made tight gate positioning prior to cell-sorting impossible and any further analysis strongly susceptible to even minute contamination. We thus devised a single-cell culture strategy adapted from the Kitamura's culture system (Nojima et al., 2011) to validate the specificity of sorted cells **(Figure 1A** and **Figure S1B)**. Throughout this study, this strategy was used to select cells for further VDJ analysis and correct gating strategies *a posteriori* for single-cell sequencing cell-sorting and FACS analysis of markers of interest using index-sorting information. Such system also allowed us to confirm the presence of true B5-specific B cells in the splenic IgG$^+$ (**Figure 1B** and **Table S1**), but not IgM$^+$CD27$^+$ or IgA$^+$ (**Figure 1C** and **Figure S1C**), MBC compartment of close to 85% of donors born before 1970 whom we could test (56 out of 66). And the estimated frequency of these cells appeared strikingly steady over three decades of life (mean = 0.012% ± 0.002 (SEM)), more than forty years post initial vaccination. Conversely, no B5-specific IgG$^+$ MBCs could be detected from the spleen of any of the 8 organ donors born after 1977 whom we could test, in line with previous ELISPOT or limited dilution assays on PBMCs and spleen of non-vaccinated individuals (Amanna and Slifka, 2006; Crotty et al., 2003; Mamani-Matsuda et al., 2008). These results confirm the exceptional longevity of such MBCs and the fact that cross-reactivation by related

Orthopoxvirus infections, while impossible to fully exclude (Gilchuk et al., 2016), is unlikely to explain such long-term maintenance in most donors.

Simple retrospective analysis of CD27 staining on all spleens for which we could reproducibly sort cells with over 80% purity showed a significant enrichment of B5-stained cells in the $CD27^+$ subset of $IgG^+$ MBCs **(Figure 1D,** $P < 0.0001$**)**. Culture-validated B5-specific $IgG^+$ MBCs were further found almost exclusively in the $CD73^+$ and $CD21^+$ subset of MBCs **(Figure 1E-F)**, with little to no $B5^+$ MBCs detected in the $CD21^{low}CD11c^+$ atypical/effector MBC compartment **(Figure 1E)**. CD45RB and CD69 staining, on the other hand, showed strong donor-to-donor variations with no clear distinction between total and B5-specific MBCs inside a given donor **(Figure S1D-E)**. This is in line with the overall variability in CD45RB/CD73 staining observed among spleens collected from over 40 patients aged 4 to 91 years old (**Figure S1F-H),** although one can note a steady increase in the $CD45RB^-CD73^+$ memory subset with age (**Figure S1H)**, along with the expected decrease in naive B cells (**Figure S1G**).

Collectively, these results demonstrate the existence of a stable and long-lived population of anti-Vaccinia MBCs in the $CD73^+CD21^+CD27^+$ $IgG^+$ MBC compartment of the spleen in vaccinated individuals.

**Vaccinia-specific long-lived MBCs display evidence of extended clonal selection.**

To further characterize the repertoire of long-lived Vaccinia-specific MBCs, we next performed $V_H$ sequencing, clonal clustering and functional analysis of MBC-derived monoclonal antibodies (mAbs) on validated single-cell culture wells using two complementary approaches. First, we single cell sorted and cultured B5-specific MBCs in a slightly different culture system (see **Methods**), which permits longer culture duration of memory-derived PCs and improved antibody yield in the supernatant, allowing for direct assessment of mAbs from culture supernatant (Sokal et al., 2021b; Watanabe et al., 2019). As a complementary approach, we sequenced light chains (see **Table S2**) and subsequently re-expressed the full IgG of the most representative member of each of the top clones from three donors.

B5-specific $IgG^+$ MBCs did not display public use of given $V_H$ among donors (**Figure S2A**) and consisted mostly of IgG1 (**Figure S2B**). Yet, in line with a T-cell dependent and GC-derived MBC response, they displayed clear evidence of clonal expansion and somatic

hypermutation (SHM) (**Figure 2A-B**). The repertoire of B5-specific MBCs notably showed extremely reduced diversity as compared to the repertoire of MBCs a couple of months or years post vaccination against Influenza (Andrews et al., 2019; Matsuda et al., 2019), Yellow Fever (Wec et al., 2020) or SARS-CoV-2 (Sokal et al., 2021b; Wang et al., 2021), with the top five clones accounting for 61 to 84% of all sequences in all five donors analyzed (**Figure 2A** and **Figure S2C**). The top clones for each donor thus represented each from $8x10^4$ to slightly over $5x10^5$ cells in a human spleen containing an estimated $70x10^9$ lymphocytes (**Figure S2D**) (Trepel, 1974).

Diversity was further restricted at the intraclonal level, as revealed by the narrow distribution of intraclonal $V_H$ mutations (**Figure 2B**) and affinities (**Figure 2C-D**). Evolutionary tree of the major clones for each donor (**Figure 2D** and **Figure S2E**) showed clear evidence of selective sweep and subclonal competition (Horns et al., 2019), and cells bearing the exact same $V_H$ genes could reproducibly be sorted from multiple vials of the same donor in multiple cases. Most anti-B5 antibodies displayed medium to strong affinity against B5, with KD in the order of $10^{-8}$ to $10^{-10}$ M (**Figure 2C**) and all clones exhibited strong convergence at the level of affinity and CDR3 sequences (**Figure 2D-E**, **Figure S2E** and **Table S2B**).

Collectively, these results suggest extensive clonal selection and a role for BCR affinity in the initial selection and/or survival of long-lived MBCs.

**Vaccinia-specific long-lived MBCs are enriched in a splenic CD21$^{hi}$ IgG$^+$ MBC subset.**

Selection of long-lived MBCs as a separate MBC lineage during the early stages of an immune response would most likely result in a unique transcriptional signature for this subset. To test this hypothesis, we next performed single-cell RNA sequencing (scRNA-seq) on single-cell sorted B5-specific IgG$^+$ MBCs, as well as paired total IgG$^+$ MBCs and naive B cells from the spleen of six donors. The generated scRNA-seq dataset was further integrated with a previously published dataset which included splenic MBCs from three adult organ donors and three immune thrombocytopenic purpura (ITP) adult patients as well as splenic naive, GC and MBCs from four young patients with sickle cell disease (Crickx et al., 2021) (see **Table S2A**).

Unsupervised clustering analysis yielded 10 clusters **(Figure 3A-B** and see **Table S3B-C)**, which included five MBC clusters (clusters 0, 1, 3, 6, 7 and 8) and two clusters regrouping

most sorted naive B cells (cluster 2) or most sorted GC B cells (cluster 5). Two additional clusters (clusters 4 and 9) displayed mostly markers linked to poor quality or apoptosis (see **Table S3C**) and were not further explored.

Closer analysis of the six MBC clusters showed two main resting MBC clusters (cluster 0 and 1), expressing *TCF7* (Jenks et al., 2018) but separated by their mRNA expression levels of *CR2* (CD21), *MYC*, *AHNAK* or *COCH* (**Figure 3C**, **Figure S3A** and see **Table S3C**). Another memory cluster (cluster 7) displayed a DN2/effector MBC signature (Jenks et al., 2018; Lau et al., 2017; Nellore et al., 2019), which included high expression of *CD19* and *MS4A1* (CD20), low expression of CD21 (*CR2*) and unique expression of *TBX21* (Tbet), *ITGAX* (CD11c) and *FCRL3/5* (**Figure 3C** and see **Table S3C**). The last three MBC clusters (cluster 3, 6 and 8) each displayed different flavors of activation or cytokine signaling signatures, including a TNF/NF-κB/immediate early genes signature in clusters 3 (mostly young donors' MBCs) and 6 and an interferon/STAT1 signature in cluster 8 **(Figure 3C** and see **Table S3C)**. The frequencies of MBCs falling into these three clusters, however, appeared highly variable among donors (see **Table S3B**).

Going against the hypothesis of a unique signature for long-lived MBCs, $B5^+$ $IgG^+$ MBCs did not segregate as a separate cluster in this analysis and could be found in all MBC clusters (**Figure 3A**). Yet, in line with their putative generation a few decades ago, most of these long-lived anti-Vaccinia MBCs were found in the two resting MBC clusters, most of them in cluster 0 with a small, albeit significant, enrichment in this cluster as compared to total $IgG^+$ MBCs **(Figure 3B**, $P = 0.0007$**)**. Differential expression analysis between sorted $B5^+$ $IgG^+$ and total $IgG^+$ MBCs did not highlight any gene signature independent of the overall cellular distribution inside identified clusters (data not shown), confirming the absence of a unique "longevity" signature in Vaccinia-specific MBCs. Of note, fractions of long-lived anti-Vaccinia MBCs did fall into each of the "activated" memory clusters. The frequencies of $B5^+$ $IgG^+$ MBCs in these clusters, however, mostly mirrored the ones of total MBCs from the same patients **(Table S3B)**, in line with our previous results on CD69 staining on B5-specific MBCs (**Figure S1D**).

To validate such results in a broader cohort of donors, we next designed multi-parametric flow cytometry panels that would allow us to separate the main clusters found in our scRNA-seq analysis. Simply looking at CD21 (upregulated on cluster 0 MBCs) versus

CD20 expression on the main subpopulations of splenic B cells revealed, in all donors, a substantial population of $IgG^+$ MBCs displaying enhanced CD21 and CD20 expression ($CD21^{hi}CD20^{hi}$) as compared to the bulk of naive B cells (**Figure 3D**), reaching fluorescence intensities like the one of $IgD^+CD27^+$ splenic marginal zone B cells (MZB) (**Figure 3E**). Unlike $CD21^{low}CD20^{hi}$ $IgG^+$ MBCs, which also upregulate CD20, these cells did not express CD11c or Tbet (**Figure 3D**), appeared mostly absent from the blood (**Figure 3E-F** and **Figure S3B**) and accumulated in the spleen with age (**Figure 3G** and **Figure S3D**). A similar $CD21^{hi}CD20^{hi}$ population could also be detected in IgA and IgM-only memory subsets (**Figure S3C**), highlighting a putative common signature of splenic resident MBC populations. In contrast, $CD21^{low}CD20^{hi}$ DN2/effector MBCs (cluster 7) rarely exceeded a few percent of total splenic $IgG^+$ MBCs and did not seem to increase with age (**Figure S3D**). No clear population of $CD71^+$, $CD25^+$ or $CD95^+$ splenic MBCs could be detected in any of the donors but high frequencies of $CD83^+$ $IgG^+$ MBCs (marker of cluster 3), and matched $B5^+$ $IgG^+$ MBCs (HD72, **Figure S3F-G**), could be seen in a small number of donors and were often associated with high frequencies of GC B cells (in young adult donors) or PCs (in older donors) (**Figure S3D**). This thus likely reflects bystander signaling in the context of an ongoing immune response.

In line with our scRNA-seq data, *in vitro* validated $B5^+$ $IgG^+$ MBCs were mostly found in both $CD21^{int}CD20^{int}$ and $CD21^{hi}CD20^{hi}$ MBCs populations but were enriched in the later population (**Figure 3H and Figure S3E**, p=0.0371). If both populations of cells represented distinct MBC populations established early on during the GC response, one would expect divergence in the respective repertoire of $CD21^{hi}CD20^{hi}$ and $CD21^{int}CD20^{int}$ $IgG^+$ $B5^+$ cells after several decades. Re-interrogating our VDJ sequencing data (**Figure 2**) in the light of CD21 index-sorting information, however, revealed that for 26 out of the 30 clones containing more than 5 members we could detect a mix of $CD21^{hi}CD20^{hi}$ and $CD21^{int}CD20^{int}$ cells (**Figure S3I and Table S2F**), with overall similar frequencies of $CD21^{int}CD20^{int}$ for all clones of a given donor (**Figure S3H**) and random distribution on the evolutionary tree of individual clones (**Figure 3I** and **Figure S3I**).

Overall, these results argue in favor of a model in which cells can dynamically transit over time between the two major $CD21^{hi}$ and $CD21^{int}$ splenic MBC subsets. The enrichment of

long-lived $B5^+$ MBCs in the splenic memory $CD21^{hi}CD20^{hi}$ compartment nonetheless suggests a survival benefit associated with residing in particular splenic niches.

**$CD21^{hi}$ $IgG^+$ splenic MBCs exhibit a NOTCH/MYC/ETV6-driven signature.**

To better understand the relationship between these two resting splenic MBC subsets, we next compared the transcriptional signature of cells in the corresponding scRNA-seq clusters (cluster 0 and 1) with the one of naive B cells (cluster 2), focusing on donors for which we had sorted both naive and MBCs to be able to properly account for potential donor-specific variations. Rather than separate transcriptional programs (**Figure 4A** and **Figure S4A-B**), both MBCs clusters appeared to share a common transcriptional signature that separated them from naive B cells with 133 commonly upregulated genes (gene module M2, **Figure 4A**) and over 400 commonly downregulated genes (gene module M7, **Figure S4C**). In addition to this core memory signature, cluster 0 ($CD21^{hi}$) MBCs further expressed a unique signature composed of 346 genes (gene modules M0 and M1, **Figure 4A**), with cluster 1 ($CD21^{int}$) MBCs mostly demonstrating intermediate expression of part of these genes as compared to naive B cells.

Gene set enrichment analysis (GSEA, (Subramanian et al., 2005)) confirmed the gradual acquisition of a distinct signature from cluster 2 naive B cells to clusters 1 and 0 MBCs, with no detectable enriched gene set unique to cluster 1 MBCs in the performed comparisons. Multiple metabolism-associated pathways , encompassing protein synthesis, glycolysis, oxidative phosphorylation and upstream MYC activation, as well as a "NOTCH signaling in B cell lymphoma" signature (Ryan et al., 2017), appeared progressively upregulated from cluster 2 to clusters 1 and 0 (**Figure 4B-C**). The latest was associated with the upregulation of many known NOTCH2 target genes in B cells (Descatoire et al., 2014), including *CR2* (CD21), *HES1*, *HES4*, *DTX1*, *CD300A* or *MYC* (**Figure 4A**). Network inference analysis using the SCENIC pipeline (Aibar et al., 2017), equally highlighted *MYC*, *ETV6* and *HES1* as 3 of the top transcription factors (TFs) whose associated regulons appeared significantly over-expressed in cluster 0 MBCs, with low to intermediate expression in cluster 1 MBCs (**Figure 4D-E**).

To confirm these results in a context of increased sequencing depth and to validate our CD21/CD20-based gating strategy, we next performed bulk RNA and ATAC-seq on sorted $CD21^{hi}CD20^{hi}$ and $CD21^{int}CD20^{int}$ $IgG^+$ MBCs and naive B cells (**Figure 4F**). Both bulk

RNA-seq and ATAC-seq PCA analysis demonstrated a clear separation along the first principal component between naive B cells and the two sorted subsets of MBCs, accounting for close to 50% of the overall variance (**Figure 4G** and **Figure S5A)**. While the next principal components mostly highlighted donor-specific variations in each assay, sorted MBC subsets appeared nonetheless separated along the fifth (rPC5) and fourth principal component (aPC4) of each assay, with good correlation when looking at differentially expressed genes driving the separation at the epigenetic level (**Figure S5B**). Most importantly, GSEA analysis matched our scRNA-seq results, highlighting again NOTCH, MYC and metabolic pathways-associated gene sets as progressively upregulated from naive to $CD21^{hi}$ MBCs in the spleen (**Figure 4H and Figure S4E-F**), with known NOTCH, MYC and ETV6 target genes mostly upregulated in $CD21^{hi}$ $IgG^{+}$ MBCs as compared to $CD21^{int}$ $IgG^{+}$ MBCs (**Figure 4I**). The overall number of significantly differentially accessible regions, however, remained limited between both memory subsets ($n$ = 41 with increased accessibility in $CD21^{hi}$, ATAC regions module M0, and $n$ = 15 with decreased accessibility in $CD21^{hi}$, ATAC regions modules M4 and M5, **Figure S5C**). Among direct NOTCH target genes in B cells (Ryan et al., 2017), only *HES4* did appear differentially accessible at the level of the chromatin (**Figure 4J and Figure S5D**) and most other NOTCH or MYC target genes like *CR2* (CD21) did not show such regulation (**Figure 4J and Figure S5E**). This was not the case, however, when looking at both MBC subsets as compared to naive B cells. Here, clear regulation at the epigenetic level appeared to explain differential expression of many NOTCH targets (**Figure 4J**), often in association with ETV6 or MYC, as evidenced for *IL21R* or *TNFRSF13B* (TACI) (**Figure S5F-G**).
Overall, these results suggest that temporal access to NOTCH ligands or specific cellular interactions rather than a unique epigenetic status regulates most of the transcriptional signature detected in $CD21^{hi}$ $IgG^{+}$ MBCs as compared to $CD21^{int}$ $IgG^{+}$ MBCs. Different accessibility of NOTCH target genes between naive and MBCs suggests in contrast that they will respond differently to a similar NOTCH triggering.

**$CD21^{hi}$ $IgG^{+}$ splenic MBCs share partial phenotype and homing potential with splenic marginal zone B cells.**

Among the signature highlighted by our combined single cell and bulk RNA-seq transcriptomic analysis of splenic $CD21^{hi}$ $IgG^{+}$ MBCs figured numerous key B cell surface

receptors associated with BCR signaling (both activator [*CD19*, *CD20*, CR2 (CD21), *CD27* or *CD40*] and inhibitor [*CD22*, *CR1* (CD35), *CD72*, *LAIR1*, *CEACAM1* (CD66a), *CD84*, *LILR4A* (CD85g), *FCRL4*, *FCRL5* or *CD300A*]), survival (*TNFRSF13B* (TACI)), cell interaction or migration (*ICAM1* (CD54), *ITGAL* (CD11a)) **(Figure 5A** and **Table S3**). KLF2 and KLF2-induced genes (Hart et al., 2011; Lechner et al., 2021) were also downregulated in these $CD21^{hi}$ $IgG^{+}$ MBCs (**Figure 5B**), including many commonly expressed genes between cluster 1 $IgG^{+}$ memory and naive B cells (**Figure 4A**, Gene module 5: *AHNAK*, *PELI1*, *RASGRP2*, *STK38*, *EMP3*). Many of these markers were previously described as upregulated on unswitched MZBs whose development also depends on NOTCH2 signaling (Descatoire et al., 2014) and KLF2 transcription factor downregulation (Hart et al., 2011).

Using multiparametric FACS analysis, we could further validate most of the selected DEGs at the protein level. $CD21^{hi}$ $IgG^{+}$ MBCs displayed increased expression of integrins and adhesion molecules usually associated with retention in the marginal zone of the spleen (reviewed in (Cyster and Allen, 2019)), notably LFA-1(CD11a/CD18) and ICAM1(CD54), reaching expressions seen on MZB cells (**Figure 5C**). CXCR5 downregulation, also key for the relocation outside of the B cell follicle in the spleen (Cyster and Allen, 2019), appeared mostly common to all MBC populations (**Figure 5C**). $CD21^{hi}$ $IgG^{+}$ MBCs also displayed enhanced membrane expression of numerous BCR complex members listed above (**Figure S6A**), apart from CD85g, FCRL4 and FCRL5 whose expression could not be detected. Finally, NOTCH-regulated surface molecules, including NOTCH2 (**Figure 5D**), TACI (**Figure 5E**) and CD27 (**Figure S6B**) were also upregulated on $CD21^{hi}$ as compared to $CD21^{int}$ $IgG^{+}$ MBCs, as well as BAFFR and known MZB markers CD1c and TLR10. However, it should be noted that $IgG^{+}$ MBCs still displayed key differences with MZB, notably reduced CD148 and enhanced CD80 and CD86 expression (**Figure S6C**) as well as markedly different integrin β1/integrin β7 expression profiles, with total $IgG^{+}$ MBCs displaying a unique integrin $\beta1^{hi}$/integrin $\beta7^{low}$ profile among splenic B cell subsets (**Figure S6D**). This likely reflects distinct differentiation pathways or tissue of origin and accessibility to specific niches in some organs like gut associated lymphoid tissues (Gorfu et al., 2009).

Overall, these results validated the transcriptional signature identified for $CD21^{hi}$ $IgG^+$ MBCs and strongly suggested that $CD21^{hi}$ $IgG^+$ MBCs and MZB share common features related to activation status and relocation to the marginal zone outside the B cell follicle. Strong inter-donor variability could be seen for some of these markers, such as NOTCH2 (**Figure 5D** and **Figure S6E**). This donor-specific variability, however, appeared correlated with overall CD21 expression on naive B cells (**Figure S6F-G**), suggesting inter-donor differences in the availability of NOTCH ligands in the spleen.

**$CD21^{hi}$ $IgG^+$ splenic MBCs display enhanced metabolic activity.**

In addition to the NOTCH/splenic marginal zone signature, our transcriptomic data also pointed towards transient MYC activation and various increased metabolic pathways in $IgG^+$ resting MBCs subsets, raising the question of a dedicated metabolic pathway associated with MBC longevity.

Metabolic profiling of $IgG^+$ memory and naive B cells confirmed a moderate increase in basal glycolysis and oxidative phosphorylation (OXPHOS) (**Figure 6A-D**), but without any clear increased dependency on OXPHOS in MBCs (**Figure 6E and Figure S7A-B**). $IgG^+$ splenic MBCs also demonstrated a strong increase in glycolytic reserve and spare respiratory capacity as compared to naive B cells (**Figure 6A-D**), suggesting increased metabolic fitness. This was further associated with a significant increase in mitochondria amount and potential (**Figure 6F**), KREBS Cycle metabolites (**Figure 6G**) and *ex vivo* glucose import (**Figure 6H**) in all resting $IgG^+$ splenic MBCs, with an additional increase between $CD21^{hi}CD20^{hi}$ and $CD21^{int}CD20^{int}$ resting memory populations (**Figure 6F and H**). However, such overall increase in metabolic activity remained far from what can be reached upon *in vivo* activation as best reflected by glucose import (**Figure 6I**) and expression of metabolic enzyme (**Figure S7C**) in resting naive and MBC clusters as compared to GC B cells in our young donor cohort.

Both Seahorse profiling (**Figure S7D-G**) and fluxomic experiments using labeled glucose and glutamine (**Figure 6J** and **Figure S7H**) further demonstrated limited use of metabolites downstream glycolysis and glutaminolysis in the KREBS cycle in both splenic naive and MBCs. We also could not detect any significant export of lactate in both human B cell subsets, as previously reported in murine B cells (Waters et al., 2018). Instead, progressive labeling of ATP and UTP in these experiments suggested a predominant use

of glucose and glutamine as building blocks for cellular anabolism, notably ribose synthesis through the pentose phosphate pathways for glucose (**Figure 6J**) and pyrimidine biosynthesis for glutamine (**Figure S7H**).

The corollary of such results is a key dependency on fatty acid oxidation (FAO) for energy production in resting human B cell subsets. Supporting such hypothesis, Etomoxir-mediated blockade of fatty acid import in the mitochondria did lead to a strong yet equally proportional reduction of OXPHOS in both naive and $IgG^+$ MBCs (**Figure S7I-J**). Neutral lipids, stored in lipid droplets, were also detected in all subsets, with a gradual increase in both stored neutral lipids and overall cell size from naive to $CD21^{hi}$ $IgG^+$ MBCs (**Figure 6K-M**). As Etomoxir blockade of fatty acid oxidation led to a similar increase in the cytoplasmic content in neutral lipids in all subsets (**Figure S7K**), it, however, is likely that the size of the storage pool for such lipids is simply tailored to the ongoing metabolic needs of given B cell subpopulations.

Overall, our data suggest that the NOTCH/MYC signature of human splenic $CD21^{hi}$ resting MBCs is mostly driving an overall moderately enhanced metabolism, but no qualitative change in metabolic pathways used. The absence of a clearly dedicated metabolic pathway for long-lived memory B cells was further confirmed by the absence of detectable differences in metabolic activity between $B5^+$ $IgG^+$ MBCs and total splenic $IgG^+$ MBCs for all FACS-based assays that we could implement on such low cell numbers (**Figure S7L-M**).

**$IgG^+$ splenic MBCs acquire elongated telomeres that last for decades.**

An additional key requirement for long-term survival of any cell is to avoid entry into senescence. Telomeres, which protect chromosome extremities, are notably shortened upon each cellular division as well as under external stress (Rossiello et al., 2022) and this can lead to shortening of telomeres below a critical length, usually 4-5 kb. HSCs or tumor cells thus specifically re-express enzymes participating to telomere elongation, in particular TERT, the catalytic subunit of the telomerase complex (Blackburn et al., 2015). None of these enzymes, apart from NHP2, appeared significantly over-expressed at the mRNA level in resting MBCs in our scRNA-seq dataset **(Figure 7A)**. In contrast, strong expression of numerous members of the shelterin (dedicated to structure and protection of telomeres (de Lange, 2018)) and telomerase complex could be detected in actively dividing

GC B cells, in line with the previously described telomerase activity in GC B cells (Hu et al., 1997; Martens et al., 2002; Norrback et al., 2001; Weng et al., 1997). TERT transcripts could not be detected in any of the assayed cell types in our scRNA-seq dataset.

To study telomere length in long-lived MBCs, in a setting that would allow studying only a few hundred cells and allow the resolution of B cell populations beyond the simple separation of $CD27^+$ memory B cell and $CD27^-$ naive B cells (Martens et al., 2002; Son et al., 2003; Weng et al., 1997), we turned to a FISH-based assay (Benyelles et al., 2019)(**Figure 7B**). Separating $IgG^+CD27^+$ MBCs from unswitched $IgD^+CD27^+$ marginal zone B cells revealed a striking difference between the two populations in the intensity, but not number, of imaged telomere spots **(Figure 7C-E)**. The significantly increased fluorescence intensity in $IgG^+$ MBCs as compared to naive B cells suggested elongated telomere length that was further confirmed using a classical TRF assay (13.3 ± 0.4 kb versus 7.7 ± 0.6 kb, **Figure 7F)**.

Analysis of nineteen donors aged 20 to 90 years old further showed a gradual decrease in telomere length with age in naive and $IgG^+$ MBC populations **(Figure 7G)**. $B5^+CD27^+IgG^+$ MBCs displayed a slightly reduced telomere length as compared to the bulk of $CD27^+IgG^+$ MBCs in each of the six donors that we could analyze **(Figure 7H-J**), confirming their generation more than five decades ago. In all cases, however, $B5^+CD27^+IgG^+$ MBCs maintained telomere length superior to the one of naive B cells from the same donor.

Collectively, these data suggest that telomeres are selectively elongated in GC-derived switched MBCs and that such long telomeres persist for decades, allowing long-term protection against senescence in these long-lived somatic cells.

## Discussion

Immune memory in humans has been shown to extend well beyond decades, with some vaccination and natural infection settings known to offer life-long protection via serum antibodies or MBCs (Amanna, 2007; Bauer and Jilg, 2006). The ability to sort Vaccinia B5-specific long-lived MBCs with high purity put us in a unique position to study MBCs generated decades ago and to address the question of whether these long-lived MBCs represent a separate subset of MBCs in the spleen with distinct survival mechanisms.

A first important result came from analyzing telomere length in splenic B cells. In all donors analyzed, and irrespective of age, $IgG^+$ $CD27^+$ MBCs had markedly longer telomeres than naive B cells, in contrast to what has been described in memory T cells (Fali et al., 2019; Martens et al., 2002; Rufer et al., 1999). Telomeres in anti-B5 B cells were slightly shorter than the ones of total $IgG^+$ MBCs from the same donor, yet, more than 40 years after being generated, these cells still displayed longer telomeres than their naïve B cell counterparts. In the absence of telomerase activity, the length of telomeres in a somatic cell is mostly a marker of its proliferative history. It has been estimated using deuterium labeling that human CD8 memory T cells, generated by Yellow fever vaccination, presented a doubling time of over 450 days (Akondy et al., 2017). We do not have these figures for human MBCs but this number is similar to what has been described for MBCs in mouse models (Jones et al., 2015). The slow decline of telomere length with age in total $IgG^+$ MBCs and the slightly shorter telomeres in presumably older anti-Vaccinia MBCs are also in line with such a division rate. This slow erosion also favors a model in which early elongation at the naive to memory differentiation step, rather than periodical reactivation of telomerase throughout life, accounts for the telomere size seen in $IgG^+$ switched MBCs. Strong telomerase activity in GC B cells has been reported but results regarding whether this leads to elongated telomeres in generated MBCs were still controversial (Hu et al., 1997; Martens et al., 2002; Norrback et al., 2001; Son et al., 2003; Weng et al., 1997). Our data strongly suggest that the passage in GCs provides GC-derived MBCs with a reserve in telomere provision, in the 10-15kb range. This reserve appears to last for decades and gives them, in theory, the capacity to divide extensively and differentiate into PCs if confronted to their cognate pathogen while having telomere length far above senescence-prone values. We did not detect any senescence signature in anti-B5

MBCs and these cells readily proliferated and differentiated into PCs in our single-cell culture settings, as previously seen in limiting dilution or ELISPOT assays (Amanna and Slifka, 2006; Crotty et al., 2003; Mamani-Matsuda et al., 2008).

A second likely mark of GC imprinting appeared when analyzing the repertoire of anti-B5 MBCs. Only a handful of clones with limited intra-clonal diversity and a narrow range of intra-clonal affinities persisted over such an extended period, with mostly mid to high affinity antibodies (KD in the order of $10^{-8}$ to $10^{-10}$ M). We do not have a longitudinal follow up on such a repertoire, but comparison with repertoires described in other vaccinal or natural infection settings up to a year post initial priming suggests that the affinity-driven selection process of the memory pool could extend well over the first year (Andrews et al., 2019; Sokal et al., 2021b; Wang et al., 2021; Wec et al., 2020). This result implies that the antigen be present and accessible during this period. Extended presentation of antigens by follicular dendritic cells (FDCs) has been hypothesized based on limited degradation of presented antigenic complexes at their cell surface (Heesters et al., 2013, 2014; Zinkernagel, 2018). Whether FDCs inside GCs represent the only location of antigenic depots in the context of Vaccinia or other infection and vaccination settings, however, remains to be determined. It has also been reported in mice that many GC-derived MBCs present low-affinity to the original immunizing antigen (Viant et al., 2020). Our sorting strategy could have missed some of these low affinity MBC clones, although human MBCs with affinities between $10^{-7}$-$10^{-8}$ M have been sorted against proteins of approximatively the same size as B5, such as SARS-CoV-2 RBD, as a bait antigen (Sokal et al., 2021b).

A key question remains whether such selection of long-lived MBCs is also associated with an early imprinting of a unique transcriptional or metabolic profile. What seems to emerge from the analysis of MBCs generated decades ago is more along the way of a dynamic recirculation through a specific microenvironment providing the longevity signal. Like most switched MBCs, B5-specific long-lived MBCs were almost exclusively $IgG^+CD27^+CD73^+CD21^+$ and were mainly found in two resting splenic clusters expressing *TCF7*, a transcription marker associated with central memory (Jenks et al., 2018; Nellore et al., 2019) but not *TBX21* (Tbet)(Johnson et al., 2020). These two subsets could be separated based on their intermediate or high expression of *CR2* (CD21), with a constant circulation between them, as recently hypothesized by Kibler *et al*. based on bulk VDJ

repertoire analysis and *in vitro* NOTCH triggering experiments (Kibler et al., 2021). This dynamic recirculation was best exemplified by the presence of B cells belonging to both clusters in most individual B5-specific clones, although B5-specific MBCs appeared overall enriched in the $CD21^{hi}$ subset in all donors.

The transition to the $CD21^{hi}$ subset appears associated with the gradual acquisition of a NOTCH/MYC signature akin to the one described for unswitched murine and human marginal zone B cells (Descatoire et al., 2014; Gaudette et al., 2021; Sintes et al., 2017), with nevertheless some sharp differences, the most notable being the absence of CD148 membrane tyrosine phosphatase expression, the lack of a detectable mTOR signature and a much higher expression of the CD80 and CD86 costimulatory molecules. In line with the growth-promoting role of the MYC transcription factor, $CD21^{hi}$ $IgG^{+}$ MBCs also displayed a moderate increase in cell size and basal metabolic activity. Such phenotypic, transcriptomic and metabolic signature for $CD21^{hi}$ switched MBCs could *a priori* evoke a "primed" state for this subset, as suggested in previous reports on similar $CD21^{hi}$ B cell subsets (Ettinger et al., 2007; Gaudette et al., 2021; Kibler et al., 2021). However, several elements in the characterization of such $CD21^{hi}$ splenic MBC population invite us to revisit this interpretation. First, the enrichment of anti-B5 MBCs in this subset suggests a key survival benefit associated with transiting through the $CD21^{hi}$ cell state and its associated niche. This was also reflected at the level of TACI expression, a receptor for the BAFF cytokine, that has recently been linked to MBCs survival in mice (Müller-Winkler et al., 2021) and appeared to be under the direct control of NOTCH signaling in human splenic $IgG^{+}$ MBCs. Second, parallel upregulation of both activating and inhibitory members of the BCR complex could be detected and no metabolic switch could be seen, unlike true human B cell activation (Waters et al., 2018). $IgG^{+}$ splenic MBCs appear to mostly depend on fatty acid oxidation for their energy production, like their quiescent central memory $CD8^{+}$ T cell counterpart (O'Sullivan et al., 2014), and additional glucose uptake seems mostly dedicated to fueling cellular anabolism. One could propose that these $CD21^{hi}$ splenic MBCs are in a state of cellular idling (van Velthoven and Rando, 2019), balancing activation and restraint to efficiently maintain their responsiveness and fitness in the competitive microenvironment of the spleen while remaining quiescent.

As part of their distinct transcriptional signature, human $CD21^{hi}$ $IgG^+$ MBCs also displayed the integrin and chemokine profile described for optimal retention of murine MZB in the splenic marginal zone (Lu and Cyster, 2002). Only indirect data exists regarding the precise positioning of $IgG^+$ switched MBCs in the human spleen (Ettinger et al., 2007; Steiniger, 2015; Steiniger et al., 2005; Tangye et al., 1998), in part due to technical limitations in staining membrane IgG on histological sections. All reports, however, points towards a $IgD^-IgM^-CD27^+$ splenic MBC population intermixed with unswitched $IgD^+CD27^+$ marginal zone B cells, $CD3^+$ T cells, ILCs, $CD11c^+$ DCs, neutrophils and $MAdCAM^+$ stromal cells in the perifollicular area of the human spleen (Ettinger et al., 2007; Magri et al., 2014; Puga et al., 2012; Steiniger et al., 2005, 2014; Tangye et al., 1998), which resembles the splenic marginal zone (MZ) described in mice and is often labeled as such (Steiniger, 2015). Our results suggest that this area of the human spleen, which provides notable access to ICAM-1/LFA-1-mediated interactions with stromal cells and BAFF and APRIL locally produced by neutrophils (Puga et al., 2012), could serve as a key niche for splenic switched MBCs survival in addition to contributing to their reactivation (Ettinger et al., 2007; Kibler et al., 2021).

In conclusion, we propose that the contraction of the MBC pool probably lasting for a few years seems to be based on their BCR affinity for the antigen. Their journey into GC imprints them with a long-lasting potential, as best exemplified by telomere elongation. This appears to be further complemented by regular transit into a specific splenic niche providing critical stimuli allowing them to stay functionally alert up to 60-70 years after their generation.

**Limitations of the study**

Major limitations of our work are inherent to the timing and technical challenges linked with the study of such long-lived MBCs. We have focused on an in-depth analysis of the response against the sole B5 antigen and it cannot be excluded, at that stage, that different mechanisms might regulate the response against other epitopes. Additionally, studying MBCs generated more than 40 years ago has forced us to focus on donors aged 50 years or more. Many studies have already tracked the early steps of a primary MBC response in human. Our study suggests that extending such follow-up well over 1 year and to secondary

lymphoid organs might be required to fully understand the mechanism at the basis of long-lived MBCs generation in humans and overall memory longevity in the context of emerging viral threats such as SARS-CoV-2 or Monkeypox.

**Acknowledgements**

We thank Sandra Weller for her invaluable advices; Garnett Kelsoe for the MS40L$^{lo}$ human cell culture system; Alexander van Oudernaarden and Judith Vivier (Hubrecht Institute, Netherlands) for initial advices regarding scRNA-seq analysis; MetaToul (Metabolomics & Fluxomics Facitilies, Toulouse, France) and its staff members (Maud Heuillet, Floriant Bellvert and Edern Cahoreau) for carrying out the metabolomic analysis; Nicolas Goudin and Beatrice Durel (SFR Necker, Paris, France) for help regarding image acquisition and analysis; Laëtitia Kermasson (Imagine Institute, Paris, France) for help regarding the set-up of Telo-FISH assays; Christophe Quétard (SARTORIUS, France) for advice on the use of the OCTET Red instrument; Jerry W. Shay and Woodring E. Wright for the kind gift of the Muntjac cells and and Raymond-Max Aubert for his support. We also gratefully thank all coordinators involved with spleen collections at the Agence de la Biomedecine.

The following reagent was obtained through BEI Resources, NIAID, NIH: Vaccinia Virus B5R Protein (NR-746).

**Funding**:

This work was funded by the Fondation Princesse Grace, by a Mérieux grant and by ERC Advanced Grants (Memo-B and B-response). M.A.E was supported by a grant from the Fondation EDF. MetaToul is part of the national infrastructure MetaboHUB-ANR-11-INBS-0010. P.R. is a scientist from Centre National de la Recherche Scientifique (CNRS).

**Author contributions**:

Conceptualization: P.C., F.H., MA.E., T.F., CA.R., JC.W.; Data curation: P.C. and F.C.; Formal Analysis: P.C., F.H., MA.E., F.C.; L.DS., L.P. and C.Goetz.; Funding acquisition: CA.R and JC.W.; Investigation: P.C., F.H., MA.E., L.DS., L.P., C.Goetz, A.S., J.M., I.N., V.J., S.S. and P.R.; Methodology: P.C., F.H., MA.E., F.C., C.Guerrera, S.S., P.R., CA.R. and JC.W.; Project administration: P.C., CA.R., and JC.W.; Resources: M.M., A.C., P.R. and C. Guerrera ; Software: P.C and F.C.; Supervision: T.F., CA.R. and JC.W.; Validation: P.C., CA.R. and J.C.W.; Visualization: P.C. and F.C.; Writing – original draft: P.C., CA.R. and JC.W.; Writing – review & editing: all authors.

**Declaration of interests:**

M.M. received research funds from GSK and personal fees from LFB and Amgen and JC.W. received consulting fees from Institut Mérieux, all outside of the submitted work.

**Figure 1. Long-lived splenic Vaccinia-specific MBCs reside in the splenic CD73$^+$CD21$^+$CD27$^+$ IgG$^+$ B cell population.**

**(A)** Experimental scheme for the isolation and retrospective validation of sorted of anti-Vaccinia B5 MBCs from the spleen of organ donors. **(B)** Corrected frequencies of B5-specific MBCs in live IgG$^+$ CD27$^+$ MBCs plotted against donor's age. Donors born after 1977 (*n* = 8) and before 1970 (*n* = 56) are highlighted in red and white respectively. **(C)** Representative dot-plot of B5-staining (Left) and corrected frequencies of B5-specific MBCs in enriched IgG$^+$ or IgM$^+$CD27$^+$ live CD20$^+$ splenic B cells (Right, *n* = 5 donors). **(D)** Representative overlayed IgG and CD27 staining (Left) and frequencies of CD27$^+$ in B5$^+$IgG$^+$ or total IgG$^+$ live CD20$^+$ splenic B cells (Right, *n* = 18 donors). **(E)** Representative overlayed CD11c and CD21 staining (Left) and frequencies of CD21$^{low}$CD11c$^+$ in validated B5$^+$IgG$^+$ or total IgG$^+$ live CD20$^+$ splenic B cells (Right, *n* = 10 donors). **(F)** Representative CD73 staining (Left) and graph frequencies of CD73$^+$ in validated B5$^+$IgG$^+$ or total IgG$^+$ live CD20$^+$ splenic B cells (Right, *n* = 6 donors). (C-F) Wilcoxon matched-pairs signed rank test. (****$P$ < 0.0001, **$P$ < 0.01, *$P$ < 0.05). See also Figure S1 and Table S1.

**Figure 2. Vaccinia-specific long-lived MBCs display evidence of extensive clonal selection.**

**(A)** Clonal distribution for $V_H$ sequences from validated B5-specific IgG$^+$ MBCs (*n* = 5 donors). Outer blue semi-circular line indicates the proportion of sequences belonging to the top five clones for each donor. The total number of sequences is indicated at the pie center. Colored dots highlight shared clones between donors. **(B)** Number of mutations in the $V_H$ segment of B5-specific IgG$^+$ MBCs grouped by clone of size 5 or more for each donor. Mean±SEM. **(C)** Measured KD value (nM) for each tested supernatants (white, *n* = 102) or re-expressed antibodies (red, *n* = 14) from B5-specific IgG$^+$ MBCs. Mean KD (line) and total number of tested antibodies (above) per donor are shown. **(D)** Representative lineage trees for B5-specific IgG$^+$ MBC clones (dot size: number of identical $V_H$ sequences; dot color: isotype). Sequence logo representing all CDR3 inside that clone, as well as V and J calls, is added on the bottom right. Affinities from tested supernatants are

displayed on the right side of each tree in front of related sequence nodes. **(E)** Representative amino acid $V_H$ alignment for all non-identical sequences, at the nucleotidic level, from clone 11 (rank 1) of donor HD4. See also Figure S2 and Table S2.

**Figure 3. Vaccinia-specific long-lived MBCs are enriched in a splenic CD21$^{hi}$ IgG$^{+}$ MBC subset.**

**(A)** UMAP and clustering of all (Left) and individual sorted cell type (Right) among the 8326 scRNA-seq analyzed naive, GC and total or Vaccinia-specific memory B cells (*n* = 9 organ donors (HD); *n* = 4 young donors (YD) and *n* = 3 Immune thrombocytopenia (ITP) patients). **(B)** Relative cluster distribution for all sorted MBCs from indicated donor groups (top) and from donors for whom both total and Vaccinia-specific MBCs were sorted (matched donors, *n* = 6 out of 9 HD). Bar indicates mean with SEM. **(C)** Expression (scaled normalized counts) of selected genes in cells from all clusters. **(D)** Representative CD20 and CD21 staining in gated splenic naive and IgG$^{+}$ MBCs, with frequencies and gating strategies for CD21$^{hi}$CD20$^{hi}$, CD21$^{int}$CD20$^{int}$ and CD21$^{lo}$CD20$^{hi}$ populations (left). Representative overlayed CD11c (right, up) and Tbet staining (right, bottom) in indicated splenic naive and IgG$^{+}$ memory populations. **(E)** Representative overlayed CD21 staining in gated circulating (PBMCs) or splenic naive, CD27$^{+}$IgD$^{+}$ marginal zone (MZB) and IgG$^{+}$ MBCs. **(F)** Frequencies of naive, MZB and IgG$^{+}$ memory in B cells (left) and of indicated subpopulation in IgG$^{+}$ MBCs (right) from total PBMCs or spleen of organ donors (*n* = 7). **(G)** Frequencies of CD21$^{hi}$CD20$^{hi}$ in splenic IgG$^{+}$ MBCs plotted against donor's age (*n* = 42 donors). Linear regression and 95% confidence intervals are shown. **(H)** Representative overlayed CD21 and CD20 staining (left) and graph showing the frequencies of CD21$^{hi}$CD20$^{hi}$ in validated B5$^{+}$IgG$^{+}$ or total IgG$^{+}$ live CD20$^{+}$ splenic B cells (right, *n* = 10 donors). **(I)** Representative lineage trees for B5-specific IgG$^{+}$ MBC clones (dot size: number of identical $V_H$ sequence; dot color: index-sorting phenotype). (B) Ordinary two-way ANOVA (top) and repeated measure two-way ANOVA (bottom) with all comparisons made as compared to the "Mem HD" group. (F) Multiple and (H) single Wilcoxon matched-pairs signed rank test with FDR correction for multiple comparisons). (****$P$ < 0.0001, ***$P$ < 0.001, **$P$ < 0.01, *$P$ < 0.05). See also Figure S3 and Table S3.

**Figure 4. CD21$^{hi}$ IgG$^{+}$ splenic MBCs exhibit a NOTCH/MYC/ETV6-driven signature.**

**(A)** scRNA-seq expression data for all donors with matched naive and memory populations and for all genes significantly upregulated in one of the two quiescent IgG$^{+}$ memory clusters (clusters 0 and 1) in one of the three following comparisons: cluster 0 versus 1, cluster 0 versus 2 and cluster 1 versus 2. Row-scaled pseudobulk expression averaged by cluster and donor is displayed and genes belonging to the HALLMARK_MYC_Targets_v1 (black lines) and RYAN_NOTCH_DIRECT genesets (red lines and gene labels, (Ryan et al., 2017)) are highlighted. **(B)** preranked Geneset Enrichment Analysis (GSEA) results for all three comparisons performed in (A) and all genesets with a NES>1.5 and FDR<0.01 in one of the 3 comparisons. **(C)** Representative enrichment plots for the comparison of cluster 0 versus cluster 1. **(D)** Scaled expression (row-normalized area under the curve (AUC) score) of the topmost significantly up-regulated SCENIC regulons in indicated clusters. **(E)** Overlayed AUC score for MYC, ETV6 and HES1 regulons in cells from indicated clusters. **(F-J)** Isolation of paired splenic naive, CD21$^{int}$ and CD21$^{hi}$ IgG$^{+}$ MBC samples from organ donors ($n$ = 4) for bulk RNA-seq and ATAC-seq analysis. (F) Gating strategy, (G) PCA analysis of bulk RNA-seq expression data, (H) representative GSEA enrichment plot, (I) log2 of the fold change (Log2FC) in RNA expression for differentially expressed genes in the comparison of sorted CD21$^{hi}$CD20$^{hi}$ and CD21$^{int}$CD20$^{int}$ IgG$^{+}$ MBCs and (J) row-scaled RNA-seq expression data for all genes of the RYAN_NOTCH_DIRECT geneset detected as differentially expressed in one of the three comparisons: CD21$^{hi}$ versus CD21$^{int}$, CD21$^{hi}$ versus naives and CD21$^{int}$ versus naives. Log2FC in accessibility at the most differentially accessible NOTCH binding regions identified in our bulk ATAC-seq data for each individual gene are displayed on the right of the heatmap for all three comparisons. See also Figure S4, Figure S5 and Table S3.

**Figure 5. CD21$^{hi}$ IgG$^{+}$ splenic MBCs share partial phenotype and homing potential with splenic marginal zone B cells.**

**(A)** scRNA-seq expression (scaled normalized counts) of selected genes coding for integrins, chemokine receptors and positive and negative regulator of BCR signaling in

cluster 0 ($CD21^{hi}$), 1 ($CD21^{int}$) and 2 (Naives). **(B)** Enrichment plots for HART_$KLF2^{-/-}$ FoB_DN geneset (Hart et al., 2011) in the comparison of cluster 0 versus cluster 1 (scRNA-seq) and sorted splenic $CD21^{hi}CD20^{hi}$ versus $CD21^{int}CD20^{int}$ $IgG^+$ MBCs (bulk RNA-seq). **(C-E)** Representative overlayed stainings (top) and median fluorescence intensities (medianFI) for indicated markers (bottom) in gated splenic naive, $CD21^{int}$ or $CD21^{hi}$ $IgG^+$ MBCs (gated as in **Figure 3D**) and $IgD^+CD27^+$ marginal zone B cells (MZB) ($n$ = 7-10 HD donors). A non-parametric Friedman test with FDR correction for multiple comparisons. (****$P$ < 0.0001, ***$P$ < 0.001, **$P$ < 0.01, *$P$ < 0.05). See also Figure S6.

**Figure 6. $CD21^{hi}$ $IgG^+$ splenic MBCs display enhanced metabolic activity.**

**(A)** Representative Seahorse XF Gluco stress test's extracellular acidification rate (ECAR) results and **(B)** calculated basal glycolysis, glycolytic activity and glycolytic reserve for sorted splenic naive and $IgG^+$ MBCs ($n$ = 5 HD donors). **(C)** Representative Seahorse XF Mito stress test's oxygen consumption rate (OCR) results; **(D)** calculated basal respiration, maximal respiration and spare capacity and **(E)** calculated OCR/ECAR ratio prior to oligomycin addition for sorted splenic naïve and $IgG^+$ MBCs ($n$ = 5 donors). (A-E) Mean±SEM. **(F)** Representative overlayed histograms (top) and graph showing the fold change in TMRE and MitoID median fluorescence intensities (bottom) between splenic naive and $CD21^{hi}$ or $CD21^{int}$ $IgG^+$ MBCs (gated as in **Figure 3D**, $n$ = 8 HD donors). **(G)** row-scaled UHPLC-MS quantification of basal expression of KREBS cycle metabolites between splenic naive and total $IgG^+$ MBCs ($n$ = 3 HD donors). **(H)** Representative overlayed histograms (left) and graph showing the fold change in 2-NBDG incorporation (right) between splenic naive and $CD21^{hi}$ or $CD21^{int}$ $IgG^+$ MBCs ($n$ = 8 HD donors). **(I)** Representative overlayed histograms showing 2-NBDG incorporation in splenic naive, $CD21^{hi}$ or $CD21^{int}$ $IgG^+$ memory and GC B cells from young donors ($n$ = 4 YD donors). **(J)** Isotopomer distribution (from no labelled carbon (black, M+0) to six (yellow, M+6)) in all detected metabolites from splenic naive and total $IgG^+$ MBCs at 0, 1 and 6 hours post incubation with labelled $^{13}$C-Glucose ($n$ = 3 HD donors). **(K)** Representative overlayed histograms (left) and graph showing the fold change in NileRed median fluorescence intensities (right) between splenic naive and $CD21^{hi}$ or $CD21^{int}$ $IgG^+$ MBCs ($n$ = 8 HD donors). **(L)** Representative confocal image of NileRed stained $CD21^{hi}$ $IgG^+$ MBCs. **(M)**

Representative overlayed FSC and SSC fluorescence intensities in splenic naive and $CD21^{hi}$ or $CD21^{int}$ $IgG^+$ MBCs. (E) Wilcoxon matched-pairs signed rank test. (B, D, F, H, K) Repeated measure two-way ANOVA with FDR correction for multiple comparisons. (****$P < 0.0001$, ***$P < 0.001$, **$P < 0.01$, *$P < 0.05$). See also Figure S7.

**Figure 7. $IgG^+$ splenic MBCs exhibit elongated telomeres that last for decades.**

**(A)** scRNA-seq expression (scaled normalized counts) of detected genes coding for members of the shelterin complex or linked to telomerase biogenesis/activity and MKI67 and signature score for G2M and S cell-cycle phases in cluster 0 ($CD21^{hi}$), 1 ($CD21^{int}$), 2 (Naives) and 5 (GC). **(B)** Representative TeloFish staining in a $B5^+$ $IgG^+$ splenic MBCs (top) and an internal control Muntjac cell (bottom). **(C)** Median number of TeloFish spots detected per cell of each sorted cell type for each donor analyzed. **(D)** Representative distribution of TeloFish spot intensities (ratio over average intensity of spots in Muntjac cells), and **(E)** variation in average intensity per spots as compared to naive B cells from the same donor, in indicated subsets ($n$ = 19 HD donors). **(F)** Representative gel for telomere restriction fragment (TRF) analysis (left) and estimated telomere length (right) in indicated subsets ($n$ = 4 HD donors). **(G)** Average intensity per spots in indicated subsets compared to donors age, ($n$ = 19 HD donors). Linear regression and 95% confidence intervals are shown. **(H-J)** Representative TeloFish staining (H), representative distribution of TeloFish spots intensities (I) and variation in average intensity per spots as compared to naive B cells from the same donor, in indicated subsets (J) ($n$ = 6 HD donors). (D, I) Kruskal-Wallis test and (C, E, F, J) Repeated measures one-way ANOVA with FDR correction for multiple comparisons. (****$P < 0.0001$, ***$P < 0.001$, **$P < 0.01$, *$P <$ 0.05, n.s. non significant).

## References


Aibar, S., González-Blas, C.B., Moerman, T., Huynh-Thu, V.A., Imrichova, H., Hulselmans, G., Rambow, F., Marine, J.-C., Geurts, P., Aerts, J., et al. (2017). SCENIC: single-cell regulatory network inference and clustering. Nat. Methods *14*, 1083–1086. https://doi.org/10.1038/nmeth.4463.

Akondy, R.S., Fitch, M., Edupuganti, S., Yang, S., Kissick, H.T., Li, K.W., Youngblood, B.A., Abdelsamed, H.A., McGuire, D.J., Cohen, K.W., et al. (2017). Origin and differentiation of human memory CD8 T cells after vaccination. Nature *552*, 362–367. https://doi.org/10.1038/nature24633.

Albagli-Curiel, O., Lecluse, Y., Pognonec, P., Boulukos, K.E., and Martin, P. (2007). A new generation of pPRIG-based retroviral vectors. BMC Biotechnol. *7*, 85. https://doi.org/10.1186/1472-6750-7-85.

Aldaz-Carroll, L., Whitbeck, J.C., Ponce de Leon, M., Lou, H., Hirao, L., Isaacs, S.N., Moss, B., Eisenberg, R.J., and Cohen, G.H. (2005). Epitope-Mapping Studies Define Two Major Neutralization Sites on the Vaccinia Virus Extracellular Enveloped Virus Glycoprotein B5R. J. Virol. *79*, 6260–6271. https://doi.org/10.1128/JVI.79.10.6260-6271.2005.

Amanna, I.J. (2007). Duration of Humoral Immunity to Common Viral and Vaccine Antigens. N. Engl. J. Med. 13. .

Amanna, I.J., and Slifka, M.K. (2006). Quantitation of rare memory B cell populations by two independent and complementary approaches. J. Immunol. Methods *317*, 175–185. https://doi.org/10.1016/j.jim.2006.09.005.

Andrews, S.F., Chambers, M.J., Schramm, C.A., Plyler, J., Raab, J.E., Kanekiyo, M., Gillespie, R.A., Ransier, A., Darko, S., Hu, J., et al. (2019). Activation Dynamics and Immunoglobulin Evolution of Pre-existing and Newly Generated Human Memory B cell Responses to Influenza Hemagglutinin. Immunity *51*, 398-410.e5. https://doi.org/10.1016/j.immuni.2019.06.024.

Bauer, T., and Jilg, W. (2006). Hepatitis B surface antigen-specific T and B cell memory in individuals who had lost protective antibodies after hepatitis B vaccination. Vaccine *24*, 572–577. https://doi.org/10.1016/j.vaccine.2005.08.058.

Benyelles, M., Episkopou, H., O'Donohue, M., Kermasson, L., Frange, P., Poulain, F., Burcu Belen, F., Polat, M., Bole-Feysot, C., Langa-Vives, F., et al. (2019). Impaired telomere integrity and rRNA biogenesis in PARN-deficient patients and knock-out models. EMBO Mol. Med. *11*. https://doi.org/10.15252/emmm.201810201.

Blackburn, E.H., Epel, E.S., and Lin, J. (2015). Human telomere biology: A contributory and interactive factor in aging, disease risks, and protection. Science *350*, 1193–1198. https://doi.org/10.1126/science.aab3389.

van den Brink, S.C., Sage, F., Vértesy, Á., Spanjaard, B., Peterson-Maduro, J., Baron, C.S., Robin, C., and van Oudenaarden, A. (2017). Single-cell sequencing reveals dissociation-induced gene expression in tissue subpopulations. Nat. Methods *14*, 935–936. https://doi.org/10.1038/nmeth.4437.

Buenrostro, J.D., Giresi, P.G., Zaba, L.C., Chang, H.Y., and Greenleaf, W.J. (2013). Transposition of native chromatin for fast and sensitive epigenomic profiling of open chromatin, DNA-binding proteins and nucleosome position. Nat. Methods *10*, 1213–1218. https://doi.org/10.1038/nmeth.2688.

Chen, Y., Lun, A.T.L., and Smyth, G.K. (2016). From reads to genes to pathways: differential expression analysis of RNA-Seq experiments using Rsubread and the edgeR quasi-likelihood pipeline. F1000Research *5*, 1438. https://doi.org/10.12688/f1000research.8987.2.

Crickx, E., Chappert, P., Sokal, A., Weller, S., Azzaoui, I., Vandenberghe, A., Bonnard, G., Rossi, G., Fadeev, T., Storck, S., et al. (2021). Rituximab-resistant splenic memory B cells and newly engaged naive B cells fuel relapses in patients with immune thrombocytopenia. Sci. Transl. Med. *13*, eabc3961. https://doi.org/10.1126/scitranslmed.abc3961.

Crotty, S., Felgner, P., Davies, H., Glidewell, J., Villarreal, L., and Ahmed, R. (2003). Cutting Edge: Long-Term B Cell Memory in Humans after Smallpox Vaccination. J. Immunol. *171*, 4969–4973. https://doi.org/10.4049/jimmunol.171.10.4969.

Cyster, J.G., and Allen, C.D.C. (2019). B Cell Responses: Cell Interaction Dynamics and Decisions. Cell *177*, 524–540. https://doi.org/10.1016/j.cell.2019.03.016.

Davis, C.W., Jackson, K.J.L., McElroy, A.K., Halfmann, P., Huang, J., Chennareddy, C., Piper, A.E., Leung, Y., Albariño, C.G., Crozier, I., et al. (2019). Longitudinal Analysis of the Human B Cell Response to Ebola Virus Infection. Cell *177*, 1566-1582.e17. https://doi.org/10.1016/j.cell.2019.04.036.

Descatoire, M., Weller, S., Irtan, S., Sarnacki, S., Feuillard, J., Storck, S., Guiochon-Mantel, A., Bouligand, J., Morali, A., Cohen, J., et al. (2014). Identification of a human splenic marginal zone B cell precursor with NOTCH2-dependent differentiation properties. J. Exp. Med. *211*, 987–1000. https://doi.org/10.1084/jem.20132203.

Dobin, A., Davis, C.A., Schlesinger, F., Drenkow, J., Zaleski, C., Jha, S., Batut, P., Chaisson, M., and Gingeras, T.R. (2013). STAR: ultrafast universal RNA-seq aligner. Bioinformatics *29*, 15–21. https://doi.org/10.1093/bioinformatics/bts635.

Ettinger, R., Sims, G.P., Robbins, R., Withers, D., Fischer, R.T., Grammer, A.C., Kuchen, S., and Lipsky, P.E. (2007). IL-21 and BAFF/BLyS Synergize in Stimulating Plasma Cell Differentiation from a Unique Population of Human Splenic Memory B Cells. J. Immunol. *178*, 2872–2882. https://doi.org/10.4049/jimmunol.178.5.2872.

Fali, T., Papagno, L., Bayard, C., Mouloud, Y., Boddaert, J., Sauce, D., and Appay, V. (2019). New Insights into Lymphocyte Differentiation and Aging from Telomere Length and Telomerase Activity Measurements. J. Immunol. *202*, 1962–1969. https://doi.org/10.4049/jimmunol.1801475.

Feng, J., Liu, T., Qin, B., Zhang, Y., and Liu, X.S. (2012). Identifying ChIP-seq enrichment using MACS. Nat. Protoc. *7*, 1728–1740. https://doi.org/10.1038/nprot.2012.101.

Fenner, F., Arita, I., Henderson, D.A., Jezek, Z., and Ladnyi, I.D. (1988). Smallpox and its Eradication (World Health Organisation, Geneva).

Foglierini, M., Pappas, L., Lanzavecchia, A., Corti, D., and Perez, L. (2020). AncesTree: An interactive immunoglobulin lineage tree visualizer. PLOS Comput. Biol. *16*, e1007731. https://doi.org/10.1371/journal.pcbi.1007731.

Gaebler, C., Wang, Z., Lorenzi, J.C.C., Muecksch, F., Finkin, S., Tokuyama, M., Cho, A., Jankovic, M., Schaefer-Babajew, D., Oliveira, T.Y., et al. (2021). Evolution of antibody immunity to SARS-CoV-2. Nature *591*, 639–644. https://doi.org/10.1038/s41586-021-03207-w.

Gaudette, B.T., Roman, C.J., Ochoa, T.A., Gómez Atria, D., Jones, D.D., Siebel, C.W., Maillard, I., and Allman, D. (2021). Resting innate-like B cells leverage sustained Notch2/mTORC1 signaling to achieve rapid and mitosis-independent plasma cell differentiation. J. Clin. Invest. *131*, e151975. https://doi.org/10.1172/JCI151975.

Gilchuk, I., Gilchuk, P., Sapparapu, G., Lampley, R., Singh, V., Kose, N., Blum, D.L., Hughes, L.J., Satheshkumar, P.S., Townsend, M.B., et al. (2016). Cross-Neutralizing and Protective Human Antibody Specificities to Poxvirus Infections. Cell *167*, 684-694.e9. https://doi.org/10.1016/j.cell.2016.09.049.

Glass, D.R., Tsai, A.G., Oliveria, J.P., Hartmann, F.J., Kimmey, S.C., Calderon, A.A., Borges, L., Glass, M.C., Wagar, L.E., Davis, M.M., et al. (2020). An Integrated Multi-omic Single-Cell Atlas of Human B Cell Identity. Immunity *53*, 217-232.e5. https://doi.org/10.1016/j.immuni.2020.06.013.

Goel, R.R., Painter, M.M., Apostolidis, S.A., Mathew, D., Meng, W., Rosenfeld, A.M., Lundgreen, K.A., Reynaldi, A., Khoury, D.S., Pattekar, A., et al. (2021). mRNA vaccines induce durable immune memory to SARS-CoV-2 and variants of concern. Science *374*, abm0829. https://doi.org/10.1126/science.abm0829.

Gorfu, G., Rivera-Nieves, J., and Ley, K. (2009). Role of Beta7 Integrins in Intestinal Lymphocyte Homing and Retention. Curr. Mol. Med. *9*, 836–850. https://doi.org/10.2174/156652409789105525.

Grün, D., Kester, L., and van Oudenaarden, A. (2014). Validation of noise models for single-cell transcriptomics. Nat. Methods *11*, 637–640. https://doi.org/10.1038/nmeth.2930.

Gu, Z., Eils, R., and Schlesner, M. (2016). Complex heatmaps reveal patterns and correlations in multidimensional genomic data. Bioinformatics *32*, 2847–2849. https://doi.org/10.1093/bioinformatics/btw313.

Gupta, N.T., Vander Heiden, J.A., Uduman, M., Gadala-Maria, D., Yaari, G., and Kleinstein, S.H. (2015). Change-O: a toolkit for analyzing large-scale B cell immunoglobulin repertoire sequencing data: Table 1. Bioinformatics *31*, 3356–3358. https://doi.org/10.1093/bioinformatics/btv359.

Hafemeister, C., and Satija, R. (2019). Normalization and variance stabilization of single-cell RNA-seq data using regularized negative binomial regression. Genome Biol. *20*, 296. https://doi.org/10.1186/s13059-019-1874-1.

Hammarlund, E., Lewis, M.W., Hansen, S.G., Strelow, L.I., Nelson, J.A., Sexton, G.J., Hanifin, J.M., and Slifka, M.K. (2003). Duration of antiviral immunity after smallpox vaccination. Nat. Med. *9*, 1131–1137. https://doi.org/10.1038/nm917.

Hart, G.T., Wang, X., Hogquist, K.A., and Jameson, S.C. (2011). Krüppel-like factor 2 (KLF2) regulates B-cell reactivity, subset differentiation, and trafficking molecule expression. Proc. Natl. Acad. Sci. *108*, 716–721. https://doi.org/10.1073/pnas.1013168108.

Hashimshony, T., Senderovich, N., Avital, G., Klochendler, A., de Leeuw, Y., Anavy, L., Gennert, D., Li, S., Livak, K.J., Rozenblatt-Rosen, O., et al. (2016). CEL-Seq2: sensitive highly-multiplexed single-cell RNA-Seq. Genome Biol. *17*, 77. https://doi.org/10.1186/s13059-016-0938-8.

Heesters, B.A., Chatterjee, P., Kim, Y.-A., Gonzalez, S.F., Kuligowski, M.P., Kirchhausen, T., and Carroll, M.C. (2013). Endocytosis and Recycling of Immune Complexes by Follicular Dendritic Cells Enhances B Cell Antigen Binding and Activation. Immunity *38*, 1164–1175. https://doi.org/10.1016/j.immuni.2013.02.023.

Heesters, B.A., Myers, R.C., and Carroll, M.C. (2014). Follicular dendritic cells: dynamic antigen libraries. Nat. Rev. Immunol. *14*, 495–504. https://doi.org/10.1038/nri3689.

Hoehn, K.B., Pybus, O.G., and Kleinstein, S.H. (2020). Phylogenetic analysis of migration, differentiation, and class switching in B cells (bioRxiv. doi: 10.1101/2020.05.30.124446).

Horns, F., Vollmers, C., Dekker, C.L., and Quake, S.R. (2019). Signatures of selection in the human antibody repertoire: Selective sweeps, competing subclones, and neutral drift. Proc. Natl. Acad. Sci. *116*, 1261–1266. https://doi.org/10.1073/pnas.1814213116.

Hu, B.T., Lee, S.C., and Ryan, D.H. (1997). Telomerase is up-regulated in human germinal center B cells in vivo and can be re-expressed in memory B cells activated in vitro. J. Immunol. *159*, 1068–1071. .

Jenks, S.A., Cashman, K.S., Zumaquero, E., Marigorta, U.M., Patel, A.V., Wang, X., Tomar, D., Woodruff, M.C., Simon, Z., Bugrovsky, R., et al. (2018). Distinct Effector B Cells Induced by Unregulated Toll-like Receptor 7 Contribute to Pathogenic Responses in Systemic Lupus Erythematosus. Immunity *49*, 725-739.e6. https://doi.org/10.1016/j.immuni.2018.08.015.

Johnson, J.L., Rosenthal, R.L., Knox, J.J., Myles, A., Naradikian, M.S., Madej, J., Kostiv, M., Rosenfeld, A.M., Meng, W., Christensen, S.R., et al. (2020). The Transcription Factor T-bet Resolves Memory B Cell Subsets with Distinct Tissue Distributions and Antibody Specificities in Mice and Humans. Immunity *52*, 842-855.e6. https://doi.org/10.1016/j.immuni.2020.03.020.

Jones, D.D., Wilmore, J.R., and Allman, D. (2015). Cellular Dynamics of Memory B Cell Populations: IgM $^{+}$ and IgG $^{+}$ Memory B Cells Persist Indefinitely as Quiescent Cells. J. Immunol. *195*, 4753–4759. https://doi.org/10.4049/jimmunol.1501365.

Kibler, A., Budeus, B., Homp, E., Bronischewski, K., Berg, V., Sellmann, L., Murke, F., Heinold, A., Heinemann, F.M., Lindemann, M., et al. (2021). Systematic memory B cell archiving and random display shape the human splenic marginal zone throughout life. J. Exp. Med. *218*, e20201952. https://doi.org/10.1084/jem.20201952.

Kim, W., Zhou, J.Q., Horvath, S.C., Schmitz, A.J., Sturtz, A.J., Lei, T., Liu, Z., Kalaidina, E., Thapa, M., Alsoussi, W.B., et al. (2022). Germinal centre-driven maturation of B cell response to mRNA vaccination. Nature https://doi.org/10.1038/s41586-022-04527-1.

King, H.W., Orban, N., Riches, J.C., Clear, A.J., Warnes, G., Teichmann, S.A., and James, L.K. (2021). Single-cell analysis of human B cell maturation predicts how antibody class switching shapes selection dynamics. Sci. Immunol. *6*, eabe6291. https://doi.org/10.1126/sciimmunol.abe6291.

Kneitz, C., Goller, M., Wilhelm, M., Mehringer, C., Wohlleben, G., Schimpl, A., and Tony, H.-P. (1999). Inhibition of T cell/B cell interaction by B-CLL cells. Leukemia *13*, 98–104. https://doi.org/10.1038/sj.leu.2401235.

Korsunsky, I., Millard, N., Fan, J., Slowikowski, K., Zhang, F., Wei, K., Baglaenko, Y., Brenner, M., Loh, P., and Raychaudhuri, S. (2019). Fast, sensitive and accurate

integration of single-cell data with Harmony. Nat. Methods *16*, 1289–1296. https://doi.org/10.1038/s41592-019-0619-0.

de Lange, T. (2018). Shelterin-Mediated Telomere Protection. Annu. Rev. Genet. *52*, 223–247. https://doi.org/10.1146/annurev-genet-032918-021921.

Langmead, B., Trapnell, C., Pop, M., and Salzberg, S.L. (2009). Ultrafast and memory-efficient alignment of short DNA sequences to the human genome. Genome Biol. *10*, R25. https://doi.org/10.1186/gb-2009-10-3-r25.

Lantto, J., Haahr Hansen, M., Rasmussen, S.K., Steinaa, L., Poulsen, T.R., Duggan, J., Dennis, M., Naylor, I., Easterbrook, L., Bregenholt, S., et al. (2011). Capturing the Natural Diversity of the Human Antibody Response against Vaccinia Virus. J. Virol. *85*, 1820–1833. https://doi.org/10.1128/JVI.02127-10.

Lau, D., Lan, L.Y.-L., Andrews, S.F., Henry, C., Rojas, K.T., Neu, K.E., Huang, M., Huang, Y., DeKosky, B., Palm, A.-K.E., et al. (2017). Low CD21 expression defines a population of recent germinal center graduates primed for plasma cell differentiation. Sci. Immunol. *2*, eaai8153. https://doi.org/10.1126/sciimmunol.aai8153.

Lechner, M., Engleitner, T., Babushku, T., Schmidt-Supprian, M., Rad, R., Strobl, L.J., and Zimber-Strobl, U. (2021). Notch2-mediated plasticity between marginal zone and follicular B cells. Nat. Commun. *12*, 1111. https://doi.org/10.1038/s41467-021-21359-1.

Liao, Y., Smyth, G.K., and Shi, W. (2013). The Subread aligner: fast, accurate and scalable read mapping by seed-and-vote. Nucleic Acids Res. *41*, e108–e108. https://doi.org/10.1093/nar/gkt214.

Love, M.I., Huber, W., and Anders, S. (2014). Moderated estimation of fold change and dispersion for RNA-seq data with DESeq2. Genome Biol. *15*, 550. https://doi.org/10.1186/s13059-014-0550-8.

Lu, T.T., and Cyster, J.G. (2002). Integrin-Mediated Long-Term B Cell Retention in the Splenic Marginal Zone. Science *297*, 409–412. https://doi.org/10.1126/science.1071632.

Luo, X.M., Maarschalk, E., O'Connell, R.M., Wang, P., Yang, L., and Baltimore, D. (2009). Engineering human hematopoietic stem/progenitor cells to produce a broadly neutralizing anti-HIV antibody after in vitro maturation to human B lymphocytes. Blood *113*, 1422–1431. https://doi.org/10.1182/blood-2008-09-177139.

Magri, G., Miyajima, M., Bascones, S., Mortha, A., Puga, I., Cassis, L., Barra, C.M., Comerma, L., Chudnovskiy, A., Gentile, M., et al. (2014). Innate lymphoid cells integrate stromal and immunological signals to enhance antibody production by splenic marginal zone B cells. Nat. Immunol. *15*, 354–364. https://doi.org/10.1038/ni.2830.

Mamani-Matsuda, M., Cosma, A., Weller, S., Faili, A., Staib, C., Garçon, L., Hermine, O., Beyne-Rauzy, O., Fieschi, C., Pers, J.-O., et al. (2008). The human spleen is a major reservoir for long-lived vaccinia virus–specific memory B cells. Blood *111*, 4653–4659. https://doi.org/10.1182/blood-2007-11-123844.

Martens, U.M., Brass, V., Sedlacek, L., Pantic, M., Exner, C., Guo, Y., Engelhardt, M., Lansdorp, P.M., Waller, C.F., and Lange, W. (2002). Telomere maintenance in human B lymphocytes: *Telomere Dynamics in B Lymphocytes*. Br. J. Haematol. *119*, 810–818. https://doi.org/10.1046/j.1365-2141.2002.03910.x.

Matsuda, K., Huang, J., Zhou, T., Sheng, Z., Kang, B.H., Ishida, E., Griesman, T., Stuccio, S., Bolkhovitinov, L., Wohlbold, T.J., et al. (2019). Prolonged evolution of the memory B cell response induced by a replicating adenovirus-influenza H5 vaccine. Sci. Immunol. *4*, eaau2710. https://doi.org/10.1126/sciimmunol.aau2710.

McCarthy, D.J., Campbell, K.R., Lun, A.T.L., and Wills, Q.F. (2017). Scater: pre-processing, quality control, normalization and visualization of single-cell RNA-seq data in R. Bioinformatics btw777. https://doi.org/10.1093/bioinformatics/btw777.

Müller-Winkler, J., Mitter, R., Rappe, J.C.F., Vanes, L., Schweighoffer, E., Mohammadi, H., Wack, A., and Tybulewicz, V.L.J. (2021). Critical requirement for BCR, BAFF, and BAFFR in memory B cell survival. J. Exp. Med. *218*, e20191393. https://doi.org/10.1084/jem.20191393.

Muraro, M.J., Dharmadhikari, G., Grün, D., Groen, N., Dielen, T., Jansen, E., van Gurp, L., Engelse, M.A., Carlotti, F., de Koning, E.J.P., et al. (2016). A Single-Cell Transcriptome Atlas of the Human Pancreas. Cell Syst. *3*, 385-394.e3. https://doi.org/10.1016/j.cels.2016.09.002.

Nellore, A., Zumaquero, E., Scharer, C.D., King, R.G., Tipton, C.M., Fucile, C.F., Mi, T., Mousseau, B., Bradley, J.E., Zhou, F., et al. (2019). Influenza-specific effector memory B cells predict long-lived antibody responses to vaccination in humans. BioRxiv DOI 101101643973 https://doi.org/DOI: 10.1101/643973.

Nguyen, D.C., Duan, M., Ali, M., Ley, A., Sanz, I., and Lee, F.E.-H. (2021). Plasma cell survival: The intrinsic drivers, migratory signals, and extrinsic regulators. Immunol. Rev. *303*, 138–153. https://doi.org/10.1111/imr.13013.

Nojima, T., Haniuda, K., Moutai, T., Matsudaira, M., Mizokawa, S., Shiratori, I., Azuma, T., and Kitamura, D. (2011). In-vitro derived germinal centre B cells differentially generate memory B or plasma cells in vivo. Nat. Commun. *2*, 465. https://doi.org/10.1038/ncomms1475.

Norrback, K.-F., Hultdin, M., Dahlenborg, K., Osterman, P., Carlsson, R., and Roos, G. (2001). Telomerase regulation and telomere dynamics in germinal centers: Telomere

dynamics in germinal centers. Eur. J. Haematol. *67*, 309–317. https://doi.org/10.1034/j.1600-0609.2001.00588.x.

Olivo-Marin, J.-C. (2002). Extraction of spots in biological images using multiscale products. Pattern Recognit. *35*, 1989–1996. https://doi.org/10.1016/S0031-3203(01)00127-3.

O'Sullivan, D., van der Windt, G.J.W., Huang, S.C.-C., Curtis, J.D., Chang, C.-H., Buck, M.D., Qiu, J., Smith, A.M., Lam, W.Y., DiPlato, L.M., et al. (2014). Memory CD8+ T Cells Use Cell-Intrinsic Lipolysis to Support the Metabolic Programming Necessary for Development. Immunity *41*, 75–88. https://doi.org/10.1016/j.immuni.2014.06.005.

Pape, K.A., Taylor, J.J., Maul, R.W., Gearhart, P.J., and Jenkins, M.K. (2011). Different B Cell Populations Mediate Early and Late Memory During an Endogenous Immune Response. Science *331*, 1203–1207. https://doi.org/10.1126/science.1201730.

Pape, K.A., Maul, R.W., Dileepan, T., Paustian, A.S., Gearhart, P.J., and Jenkins, M.K. (2018). Naive B Cells with High-Avidity Germline-Encoded Antigen Receptors Produce Persistent IgM+ and Transient IgG+ Memory B Cells. Immunity *48*, 1135-1143.e4. https://doi.org/10.1016/j.immuni.2018.04.019.

Puga, I., Cols, M., Barra, C.M., He, B., Cassis, L., Gentile, M., Comerma, L., Chorny, A., Shan, M., Xu, W., et al. (2012). B cell–helper neutrophils stimulate the diversification and production of immunoglobulin in the marginal zone of the spleen. Nat. Immunol. *13*, 170–180. https://doi.org/10.1038/ni.2194.

Rossiello, F., Jurk, D., Passos, J.F., and d'Adda di Fagagna, F. (2022). Telomere dysfunction in ageing and age-related diseases. Nat. Cell Biol. *24*, 135–147. https://doi.org/10.1038/s41556-022-00842-x.

Rufer, N., Brümmendorf, T.H., Kolvraa, S., Bischoff, C., Christensen, K., Wadsworth, L., Schulzer, M., and Lansdorp, P.M. (1999). Telomere Fluorescence Measurements in Granulocytes and T Lymphocyte Subsets Point to a High Turnover of Hematopoietic Stem Cells and Memory T Cells in Early Childhood. J. Exp. Med. *190*, 157–168. https://doi.org/10.1084/jem.190.2.157.

Ryan, R.J.H., Petrovic, J., Rausch, D.M., Zhou, Y., Lareau, C.A., Kluk, M.J., Christie, A.L., Lee, W.Y., Tarjan, D.R., Guo, B., et al. (2017). A B Cell Regulome Links Notch to Downstream Oncogenic Pathways in Small B Cell Lymphomas. Cell Rep. *21*, 784–797. https://doi.org/10.1016/j.celrep.2017.09.066.

Sanz, I., Wei, C., Jenks, S.A., Cashman, K.S., Tipton, C., Woodruff, M.C., Hom, J., and Lee, F.E.-H. (2019). Challenges and Opportunities for Consistent Classification of Human B Cell and Plasma Cell Populations. Front. Immunol. *10*, 2458. https://doi.org/10.3389/fimmu.2019.02458.

Sintes, J., Gentile, M., Zhang, S., Garcia-Carmona, Y., Magri, G., Cassis, L., Segura-Garzón, D., Ciociola, A., Grasset, E.K., Bascones, S., et al. (2017). mTOR intersects antibody-inducing signals from TACI in marginal zone B cells. Nat. Commun. *8*, 1462. https://doi.org/10.1038/s41467-017-01602-4.

Sokal, A., Chappert, P., Barba-Spaeth, G., Roeser, A., Fourati, S., Azzaoui, I., Vandenberghe, A., Fernandez, I., Meola, A., Bouvier-Alias, M., et al. (2021a). Maturation and persistence of the anti-SARS-CoV-2 memory B cell response. Cell *184*, 1201-1213.e14. https://doi.org/10.1016/j.cell.2021.01.050.

Sokal, A., Barba-Spaeth, G., Fernández, I., Broketa, M., Azzaoui, I., de La Selle, A., Vandenberghe, A., Fourati, S., Roeser, A., Meola, A., et al. (2021b). mRNA vaccination of naive and COVID-19-recovered individuals elicits potent memory B cells that recognize SARS-CoV-2 variants. Immunity *54*, 2893-2907.e5. https://doi.org/10.1016/j.immuni.2021.09.011.

Son, N.H., Joyce, B., Hieatt, A., Chrest, F.J., Yanovski, J., and Weng, N. (2003). Stable telomere length and telomerase expression from naïve to memory B-lymphocyte differentiation. Mech. Ageing Dev. *124*, 427–432. https://doi.org/10.1016/S0047-6374(03)00018-6.

Steiniger, B.S. (2015). Human spleen microanatomy: why mice do not suffice. Immunology *145*, 334–346. https://doi.org/10.1111/imm.12469.

Steiniger, B., Timphus, E.-M., Jacob, R., and Barth, P.J. (2005). CD27+ B cells in human lymphatic organs: re-evaluating the splenic marginal zone. Immunology *0*, 050920031238002. https://doi.org/10.1111/j.1365-2567.2005.02242.x.

Steiniger, B.S., Wilhelmi, V., Seiler, A., Lampp, K., and Stachniss, V. (2014). Heterogeneity of stromal cells in the human splenic white pulp. Fibroblastic reticulum cells, follicular dendritic cells and a third superficial stromal cell type. Immunology *143*, 462–477. https://doi.org/10.1111/imm.12325.

Stuart, T., Butler, A., Hoffman, P., Hafemeister, C., Papalexi, E., Mauck, W.M., Hao, Y., Stoeckius, M., Smibert, P., and Satija, R. (2019). Comprehensive Integration of Single-Cell Data. Cell *177*, 1888-1902.e21. https://doi.org/10.1016/j.cell.2019.05.031.

Subramanian, A., Tamayo, P., Mootha, V.K., Mukherjee, S., Ebert, B.L., Gillette, M.A., Paulovich, A., Pomeroy, S.L., Golub, T.R., Lander, E.S., et al. (2005). Gene set enrichment analysis: A knowledge-based approach for interpreting genome-wide expression profiles. Proc. Natl. Acad. Sci. *102*, 15545–15550. https://doi.org/10.1073/pnas.0506580102.

Sundling, C., Lau, A.W.Y., Bourne, K., Young, C., Laurianto, C., Hermes, J.R., Menzies, R.J., Butt, D., Kräutler, N.J., Zahra, D., et al. (2021). Positive selection of IgG+ over IgM+ B

cells in the germinal center reaction. Immunity *54*, 988-1001.e5. https://doi.org/10.1016/j.immuni.2021.03.013.

Tangye, S.G., Liu, Y.-J., Aversa, G., Phillips, J.H., and de Vries, J.E. (1998). Identification of Functional Human Splenic Memory B Cells by Expression of CD148 and CD27. J. Exp. Med. *188*, 1691–1703. https://doi.org/10.1084/jem.188.9.1691.

Taub, D.D., Ershler, W.B., Janowski, M., Artz, A., Key, M.L., McKelvey, J., Muller, D., Moss, B., Ferrucci, L., Duffey, P.L., et al. (2008). Immunity from Smallpox Vaccine Persists for Decades: A Longitudinal Study. Am. J. Med. *121*, 1058–1064. https://doi.org/10.1016/j.amjmed.2008.08.019.

Tiller, T., Meffre, E., Yurasov, S., Tsuiji, M., Nussenzweig, M.C., and Wardemann, H. (2008). Efficient generation of monoclonal antibodies from single human B cells by single cell RT-PCR and expression vector cloning. J. Immunol. Methods *329*, 112–124. https://doi.org/10.1016/j.jim.2007.09.017.

Trepel, F. (1974). Number and distribution of lymphocytes in man. A critical analysis. Klin. Wochenschr. *52*, 511–515. https://doi.org/10.1007/BF01468720.

Van de Sande, B., Flerin, C., Davie, K., De Waegeneer, M., Hulselmans, G., Aibar, S., Seurinck, R., Saelens, W., Cannoodt, R., Rouchon, Q., et al. (2020). A scalable SCENIC workflow for single-cell gene regulatory network analysis. Nat. Protoc. *15*, 2247–2276. https://doi.org/10.1038/s41596-020-0336-2.

van Velthoven, C.T.J., and Rando, T.A. (2019). Stem Cell Quiescence: Dynamism, Restraint, and Cellular Idling. Cell Stem Cell *24*, 213–225. https://doi.org/10.1016/j.stem.2019.01.001.

Viant, C., Weymar, G.H.J., Escolano, A., Chen, S., Hartweger, H., Cipolla, M., Gazumyan, A., and Nussenzweig, M.C. (2020). Antibody Affinity Shapes the Choice between Memory and Germinal Center B Cell Fates. Cell *183*, 1298-1311.e11. https://doi.org/10.1016/j.cell.2020.09.063.

Viant, C., Wirthmiller, T., ElTanbouly, M.A., Chen, S.T., Cipolla, M., Ramos, V., Oliveira, T.Y., Stamatatos, L., and Nussenzweig, M.C. (2021). Germinal center–dependent and –independent memory B cells produced throughout the immune response. J. Exp. Med. *218*, e20202489. https://doi.org/10.1084/jem.20202489.

Victora, G.D., and Nussenzweig, M.C. (2012). Germinal Centers. Annu. Rev. Immunol. *30*, 429–457. https://doi.org/10.1146/annurev-immunol-020711-075032.

Wang, Z., Muecksch, F., Schaefer-Babajew, D., Finkin, S., Viant, C., Gaebler, C., Hoffmann, H.-H., Barnes, C.O., Cipolla, M., Ramos, V., et al. (2021). Naturally enhanced neutralizing breadth against SARS-CoV-2 one year after infection. Nature *595*, 426–431. https://doi.org/10.1038/s41586-021-03696-9.

Watanabe, A., Su, K.-Y., Kuraoka, M., Yang, G., Reynolds, A.E., Schmidt, A.G., Harrison, S.C., Haynes, B.F., St. Clair, E.W., and Kelsoe, G. (2019). Self-tolerance curtails the B cell repertoire to microbial epitopes. JCI Insight *4*, e122551. https://doi.org/10.1172/jci.insight.122551.

Waters, L.R., Ahsan, F.M., Wolf, D.M., Shirihai, O., and Teitell, M.A. (2018). Initial B Cell Activation Induces Metabolic Reprogramming and Mitochondrial Remodeling. IScience *5*, 99–109. https://doi.org/10.1016/j.isci.2018.07.005.

Wec, A.Z., Haslwanter, D., Abdiche, Y.N., Shehata, L., Pedreño-Lopez, N., Moyer, C.L., Bornholdt, Z.A., Lilov, A., Nett, J.H., Jangra, R.K., et al. (2020). Longitudinal dynamics of the human B cell response to the yellow fever 17D vaccine. Proc. Natl. Acad. Sci. *117*, 6675–6685. https://doi.org/10.1073/pnas.1921388117.

Weisel, F.J., Zuccarino-Catania, G.V., Chikina, M., and Shlomchik, M.J. (2016). A Temporal Switch in the Germinal Center Determines Differential Output of Memory B and Plasma Cells. Immunity *44*, 116–130. https://doi.org/10.1016/j.immuni.2015.12.004.

Weisel, N.M., Weisel, F.J., Farber, D.L., Borghesi, L.A., Shen, Y., Ma, W., Luning Prak, E.T., and Shlomchik, M.J. (2020). Comprehensive analyses of B-cell compartments across the human body reveal novel subsets and a gut-resident memory phenotype. Blood *136*, 2774–2785. https://doi.org/10.1182/blood.2019002782.

Weisel, N.M., Joachim, S.M., Smita, S., Callahan, D., Elsner, R.A., Conter, L.J., Chikina, M., Farber, D.L., Weisel, F.J., and Shlomchik, M.J. (2022). Surface phenotypes of naive and memory B cells in mouse and human tissues. Nat. Immunol. *23*, 135–145. https://doi.org/10.1038/s41590-021-01078-x.

Weng, N., Granger, L., and Hodes, R.J. (1997). Telomere lengthening and telomerase activation during human B cell differentiation. Proc. Natl. Acad. Sci. *94*, 10827–10832. https://doi.org/10.1073/pnas.94.20.10827.

Wong, R., Belk, J.A., Govero, J., Uhrlaub, J.L., Reinartz, D., Zhao, H., Errico, J.M., D'Souza, L., Ripperger, T.J., Nikolich-Zugich, J., et al. (2020). Affinity-Restricted Memory B Cells Dominate Recall Responses to Heterologous Flaviviruses. Immunity *53*, 1078-1094.e7. https://doi.org/10.1016/j.immuni.2020.09.001.

Yu, X., Tsibane, T., McGraw, P.A., House, F.S., Keefer, C.J., Hicar, M.D., Tumpey, T.M., Pappas, C., Perrone, L.A., Martinez, O., et al. (2008). Neutralizing antibodies derived from the B cells of 1918 influenza pandemic survivors. Nature *455*, 532–536. https://doi.org/10.1038/nature07231.

Zhao, Y., Uduman, M., Siu, J.H.Y., Tull, T.J., Sanderson, J.D., Wu, Y.-C.B., Zhou, J.Q., Petrov, N., Ellis, R., Todd, K., et al. (2018). Spatiotemporal segregation of human

marginal zone and memory B cell populations in lymphoid tissue. Nat. Commun. *9*, 3857. https://doi.org/10.1038/s41467-018-06089-1.

Zinkernagel, R.M. (2018). What if protective immunity is antigen-driven and not due to so-called “memory” B and T cells? Immunol. Rev. *283*, 238–246. https://doi.org/10.1111/imr.12648.

## STAR Methods

### RESOURCE AVAILABILITY

#### Lead Contact

Further information and requests for resources and reagents should be directed to and will be fulfilled by the Lead Contact, Pascal Chappert (pascal.chappert@inserm.fr).

#### Materials Availability

No unique materials were generated for this study.

#### Data and Code Availability

- All scRNA-seq, RNA-seq and ATAC-seq data have been deposited in the ArrayExpress database at EMBL-EBI (www.ebi.ac.uk/arrayexpress) and are available as of the date of publication. Accession numbers are listed in the Key Resources Table. Single cell culture VDJ sequencing data reported in **Figure 2 and Figure S2** are included in **Table S2** and have been deposited as Targeted Locus Study projects at DDBJ/EMBL/GenBank are available as of the date of publication. Accession numbers are listed in the Key Resources Table. The version described in this paper is the first version, KFRA01000000-KFRE01000000.
- This paper does not report original code.
- Any additional information required to reanalyze the data reported in this paper is available from the lead contact upon request.

### EXPERIMENTAL MODEL AND SUBJECT DETAILS

#### Study participants

All healthy donors (HD) spleen and PBMCs samples used in this study were from organ donors who died from stroke or head trauma and were obtained from the Agence de la Biomédecine (PFS07-009). None of them had lymphoma or autoimmune disease and donors with positive HIV, HCV or HBV serology or known immune pathology were excluded. While we didn't have access to vaccination records from these donors, we

postulated that donors born before 1970 would likely have received at least one shot of the anti-smallpox vaccine (Vaccinia) as part of the existing vaccination requirements at the time. Conversely, donors born after 1980, and the official eradication of Smallpox, are unlikely to have been vaccinated and thus should not harbor Smallpox/Vaccinia-specific MBCs. All young donors (YD) spleen included in some of the analyses were from patients with sickle cell disease who were splenectomized between the age of 4 and 5 years. Information on the age, sex, and other clinical features of the cohort are provided in Table S1. Throughout the manuscript, all patients are referred to using the nomenclature presented in **Table S1**. No sample size calculation, randomization, or blinding were performed for this study.

This study was conducted in compliance with the Declaration of Helsinki principles and was approved by the Agence de la Biomédecine and the Institutional Review Boards Comité de Protection des Personnes (CPP) Ile-de-France II, in the context of French laws regulating organ donation. Parents from young children with sickle cell disease provided written informed consent before the collection of splenic samples.

## METHOD DETAILS

### Spleen sample processing

Immediately after splenectomy, splenic tissues were maintained at 4 °C until being crushed using a gentleMacs dissociator (Miltenyi). After filtration and 1:2 dilution by RPMI-1640 (Invitrogen), mononuclear cells were isolated by ficoll density-gradient (Ficoll Paque Plus, GE Healthcare) centrifugation at 2000 rpm for 20 min with the brakes off and then stored in liquid nitrogen. PBMCs were isolated from venous blood samples via standard density gradient centrifugation and then stored in liquid nitrogen.

### B5 labeling with Alexa488 and Alexa647

Recombinant Vaccinia Virus (WR) B5R Protein (BEI, NR-546) (Aldaz-Carroll et al., 2005) was labeled with Alexa Fluor (AF) 488 (Life technologies, A30006) or AF647 (Life technologies, A30009), according to the manufacturer's recommendations, with an additional spin filter purification step at the end.

### Flow cytometry and cell sorting

Cells were slowly thawed in RPMI-1640 (Gibco)-2% FBS (Gibco) at 37 °C and washed twice prior to counting. For simple phenotyping, 2 x $10^6$ cells per condition were stained with the fluorochrome-conjugated antibody mix of interest for 40 min at 4 °C (1:100 for BV711 anti-β7, PE anti-BAFF-R, FITC anti-BCMA, AF647 anti-CD1c, AF700 anti-CD3, PerCP anti-CD3, BUV395 anti-CD3, PE anti-CD6, APC anti-CD11a, PE anti-CD11b, PeCy7 anti-CD11c, BV605 anti-CD11c, AF700 anti-CD14, PerCP anti-CD14, BUV395 anti-CD14, AF700 anti-CD16, PerCP anti-CD16, BUV395 anti-CD16, PE anti-CD18, AF700 anti-CD19, BV711 anti-CD21, PeCy7 anti-CD21, FITC anti-CD24, PeCy7 anti-CD24, BUV737 anti-CD25, PE anti-CD29, PE anti-CD35, PerCPCy5.5 anti-CD38, BV421 anti-CD38, PeCy7 anti-CD39, PE anti-CD40, PE anti-CD45RB, AF647 anti-CD45RB, APC anti-CD49d, FITC anti-CD54, PE anti-CD69, PeCy7 anti-CD71, BV786 anti-CD71, PE anti-CD72, BUV737 anti-CD73, BV605 anti-CD73, PE anti-CD80, PE anti-CD83, PE anti-CD84, AF647 anti-CD85g, PE anti-CD119, PE anti-CD148, PE anti-CD200, APC anti-CD300a, FITC anti-CXCR5, PE anti-FCRL5, FITC anti-IgD, BV605 anti-IgM, PE anti-Notch2, APC anti-OX40L, PE anti-TACI and PE anti-TLR10, 1:50 for APCH7 anti-CD20, BV421 anti-CD27, PeCy7 anti-CD27, APC anti-CD27, PE anti-IgA, PeCF594 anti-IgD and BV510 anti-IgG, 1:25 for PE anti-CD22, PE anti-CD66a, PE anti-CD86, PE anti-CD305, APC anti-FCRL4 and FITC anti-IgA and 1:10 for APC anti-CD11c and APC anti-CD38). Cells were then washed in RPMI-1640 and fixed in 2% PFA.

Samples were acquired using a LSR Fortessa SORP (BD Biosciences). Data were analyzed with FlowJo software. Detailed gating strategies for individual markers are depicted in **Figure S1**. To account for donor-specific variations in CD21 fluorescent intensities, $CD21^{hi}CD20^{hi}$ and $CD21^{int}CD20^{int}$ gates were always set-up so that the $CD21^{hi}CD20^{hi}$ gate would encompass 5% of the naive B cell population in that sample (**Figure 3D**). For CD18, CD11b, NOTCH2, CD84, TLR10, TACI and BAFFR (**Figure 5C-E)** and for CD22, CD35, CD40, CD72, CD305, CD66a and CD6 (**Figure S6A-C**), corrected median fluorescence intensities are reported, subtracting the intensity values obtained from corresponding isotype controls.

For cell sorting of major B cell population, cells were stained using the same protocol, without the final fixation step, and then sorted on a BD FACS cell sorter Aria III (BD Biosciences, 4-way purity mode). Throughout this study naive B cells were sorted as live

$CD3^-CD14^-CD16^-CD20^+CD27^-IgD^+CD24^{mid}CD38^{mid}$, marginal zone B cells (MZB) as live $CD3^-CD14^-CD16^-CD20^+CD27^+IgD^+$ and $IgG^+$ switched MBCs ($IgG^+$ memory) as live $CD3^-CD14^-CD16^-CD20^+CD27^+IgG^+$, further subdivided as $CD21^{hi}CD20^{hi}$ and $CD21^{int}CD20^{int}$ (upper and lower 30% of $CD21^+$ $IgG^+$ MBCs respectively, **Figure 4F**) for RNA-seq and ATAC-seq analysis.

For $B5^+$ MBCs sorting, cells were first stained for 40 min at 4 °C at $10^8$ cells/mL with PerCP-Cy5.5 anti-CD3/CD14/CD16 (1:100 each) and BV510 anti-IgG (1:50). $IgG^+CD3^-CD14^-CD16^-$ cells were first enriched on a BD FACSAria III cells sorter (Yield mode). Enriched $IgG^+$ cells were further labeled with APC-H7 anti-CD20 (1:50), BV421 anti-CD27 (1:100), AF647 B5 (3 µg), AF488 B5 (5 µg) and 7-AAD (1:100). Single MBCs ($B5^-IgG^+CD27^+$ or $B5^+IgG^+CD27^+$) were then sorted directly on appropriate feeder cells at 37 °C on a BD FACSAria III (0-16-0 single cell purity mode). When comparing $B5^+$ $IgG^+$ with other B cell populations, $IgG^-$ cells were enriched in parallel on the cell sorter and stained for IgD, CD24, CD27, CD38 and CD20 as described above. Naive, MZB and $IgG^+$ MBCs were then sorted from their respective $IgG^+$ or $IgG^-$ fractions. To validate phenotype of interest on $B5^+$ switched MBCs, additional markers were added to our staining panel on enriched $IgG^+$ cells: BV711 anti-CD21 (1:100), PE anti-CD83/CD69 or CD45RB (1:100 each), BV605 anti-CD73 (1:100). Analysis was refined *a posteriori* using index sorting for each single cell validated in subsequent culture and ELISA. To assess the frequencies of $B5^+$ MBCs in the $IgM^+CD27^+$ or $IgA^+$ populations, the protocol was adapted to add BV421 anti-CD27, PE anti-IgA and BV605 anti-IgM antibodies (1:100 each) in the first staining mix and start with a parallel enrichment of the main isotype-switched or unswitched MBC populations ($IgG^+CD3^-CD14^-CD16^-$, $IgA^+CD3^-CD14^-CD16^-$ and $IgM^+CD27^+CD3^-CD14^-CD16^-$ respectively).

For metabolic staining, 2 x $10^6$ cells per condition were either directly stained with the fluorochrome-conjugated antibody mix of interest for 40 min at 4 °C or, when also analysing $B5^+IgG^+$ MBCs, $IgG^+CD3^-CD14^-CD16^-$ cells were pre-enriched on a BD FACSAria III (Yield mode). For 2-NBDG incorporation, stained cells were first washed twice with glucose-free RPMI-1640. Cells were then incubated 30 min at 37 °C in glucose free RPMI with NBDG (2-(N-(7-Nitrobenz-2-oxa-1,3-diazol-4-yl)amino)-2-deoxyglucose) 30µM (Invitrogen, Cat# N13195). For mitochondria labeling, stained cells

were incubated 30 min at 37 °C in RPMI 2% FCS with TMRE (tetramethylrhodamine, ethyl ester) at 25 nM (Thermo Fischer, Cat#T669) and Mito ID Red (1/10 000, Enzo, Cat# ENZ-51007-0100). Nile Red was directly added at 1 µg/ml (ThermoFisher, N1142) in the antibody mix. For etomoxir blockade experiments (**Figure S6K**), etomoxir (100µM) or control DMSO were added for indicated time prior to Nile Red staining.

**Single-cell culture systems**

hCD40L-expressing MS40L$^{lo}$ feeder cells expressing CD40L were obtained from G. Kelsoe (Luo et al., 2009). hCD40L$^{+}$hBAFF$^{+}$hIL-21$^{+}$ B21 feeder cells were specifically generated for this study from mouse fibroblast hCD40L-expressing L cells (Kneitz et al., 1999) (see below).

Single IgG$^{+}$ or B5$^{+}$IgG$^{+}$ switched MBCs were single cell sorted in 96-well plates seeded 24h earlier with either MS40$^{lo}$ feeders and appropriate cytokines (MS40$^{lo}$ cultures) or mitomycin-treated B21 feeders (B21 cultures). B21 cultures were left at 37 °C for 14-21 days at which point supernatants were tested for IgG and B5 specificities and cell pellets were harvested in 50 µL of RLT buffer (Qiagen) supplemented with 1% 2-mercaptoethanol and subsequently stored at -80 °C until RNA extraction and VDJ sequencing. MS40$^{lo}$ cultures were performed as previously described (Crickx et al., 2021). Briefly, cells were co-cultured at 37 °C with 5% $CO_2$ during 21 or 25 days in RPMI-1640 (Invitrogen) supplemented with 10% HyClone FBS (Thermo Scientific), 55 µM 2-mercaptoethanol, 10 mM HEPES, 1 mM sodium pyruvate, 100 units/mL penicillin, 100 µg/mL streptomycin, and MEM non-essential amino acids (all Invitrogen), with the addition of recombinant human BAFF (10 ng/ml), IL2 (50 ng/ml), IL4 (10 ng/ml), and IL21 (10 ng/ml; all Peprotech). Part of the supernatant was carefully removed at days 4, 8, 12, 15, 18, 21 and 25 and the same amount of fresh medium with cytokines was added to the cultures. After 25-29 days of single cell culture, supernatants were harvested and stored at -20 °C and cell pellets were harvested in 50 µL of RLT buffer (Qiagen) supplemented with 1% 2-mercaptoethanol and subsequently stored at -80 °C until RNA extraction and VDJ sequencing.

At the end of each parallel total IgG$^{+}$ and B5-specific MBCs single-cell culture, IgG and B5 ELISA were used to distinguish non-B/poor quality B and non-specific B cell

contaminants respectively **(Figure S1B)**. Corrected frequencies of $B5^+$ $IgG^+$ were calculated as follows: $\%B5^+_{corrected} = \%B5^+_{Observed} * (B5^+_{activation}/IgG^+_{activation}) * B5^+_{purity}$, where $B5^+_{activation}$ and $IgG^+_{activation}$ correspond to the frequencies of $IgG^+$ wells at the end of the culture in sorted $B5^+IgG^+$ and control total $IgG^+$ MBCs plates respectively and $B5^+_{purity}$ correspond to the frequency of $B5^+$ wells among $IgG^+$ wells from sorted $B5^+IgG^+$ MBCs.

**Generation of retroviral expression vectors for human BAFF (hBAFF) and human IL-21 (hIL-21)**

5 µg of total RNA extracted from human splenic mononuclear cells were reverse transcribed with random hexamers at 42 °C, using the AffinityScript Multiple Temperature cDNA Synthesis Kit (Agilent) according to manufacturer's instructions. hBAFF and hIL-21 ORFs were amplified by PCR on this cDNA with the following primers: hBAFF-For-BamHI AAGGATCCGCCGCCGATATGGATGACTCCACAGA and hBAFF-Rev GGTCACAGCAGTTTCAATGC; hIL21-For-XhoI AACTCGAGCCGCCACCATGAGATCCAGTCCTGGCAAC and IL21-Rev-BglII AAAGATCTCAGGAATCTTCACTTCCGT. PCR were performed with Phusion DNA polymerase (New England Biolabs) under the following conditions: 30 s at 98 °C; 35 cycles 10 s at 98 °C, 30 s at 60 °C (hBAFF) or 62 °C (hIL-21), 1 min at 72 °C; 4 min at 72 °C. hBAFF and hIL-21 amplicons were cloned into TOPO-TA (Life Technologies) intermediate vector and subcloned into BglII/XhoI restriction sites of pMIG (Addgene # 9044, a gift from William Hahn) and XhoI/BglII sites of pRIPChp-aHA (Albagli-Curiel et al., 2007), respectively. Sequences were checked using Sanger sequencing.

**Generation of feeder cells expressing hCD40L, hBAFF and hIL-21 (B21 feeders)**

Nonreplicative ecotropic γ-retroviral particles were produced by transient lipofection (XtremeGene 9 DNA transfection reagent; Roche) of 293T cells grown in DMEM/F-12 supplemented with 10% FCS (Hyclone) with pMIG-hBAFF or pRIPChp-aHA-hIL-21, pLTR-env, and CMV-Gag/Pol vectors (ratio 2:1:1). At 48 hr after transfection, viral supernatants were filtered through 0.45 µm Minisart High Flow filters (Sartorius) and concentrated on centrifugal filter units (100K Amicon Ultra 15; EMD Millipore). hCD40L-expressing L cells were transiently transfected with pTarget-mCAT-1 expression vector (a gift from Yoshinao Kubo, University of Nagasaki, Japan) with an Amaxa Nucleofector 2b

device (Lonza, solution R, program U-030), to allow for expression of SLC7A1 ecotropic receptor, and stably transduced 48 hr later with pMIG-hBAFF (MSCV-hBAFF-ires-EGFP) viral particles in the presence of 8 µg/mL polybrene (H9268; Sigma-Aldrich). $hCD40L^{+}hBAFF^{+}$ ($GFP^{+}$) double-positive cells were FACS-sorted after staining with PE-coupled anti-human CD154 (Sony, 2154030; diluted 1:200), and long-term expression of membrane-bound hBAFF was checked by staining with an APC-coupled anti-hCD257 (Biolegend, 366507, diluted 1:100). $hCD40L^{+}hBAFF^{+}$ cells were subsequently transduced with pRIPChp-aHA-hIL-21 (pRIP-hIL-21-ires-mCherry) retroviral particles, using the same protocol. $GFP^{+}mCherry^{+}$ cells were FACS-sorted to isolate $hCD40L^{+}hBAFF^{+}hIL\text{-}21^{+}$ triple positive L cells hereafter named B21. hBAFF and hIL-21 secretion was checked by ELISA.

**ELISA**

Total IgG and B5-specific IgG from culture supernatants were measured using homemade ELISA. ELISA 96 well plates (Thermo Fisher) were coated with either goat anti-human Ig (10 µg/ml, Invitrogen, H17000) or recombinant B5 protein (2.5 µg/ml, BEI NR-546) in sodium carbonate during 1 hr at 37 °C. After plate blocking with 5% milk in PBS for 1 hr at RT, cell culture supernatants were added for 1hr at RT. Plates were washed 5 times in PBS and were then incubated for 1 hr at RT with HRP-goat anti-human IgG (1 µg/ml, Immunotech) in 1x PBS buffer with 0.1% BSA and 0.005% Tween 20 surfactant (Bio Rad). Plates were washed 5 times in PBS and incubated with KPL SureBlue™ TMB Microwell Peroxidase substrate (Eurobio, Cat# 5120-0077) for 5-15 minutes at room temperature. The reaction was stopped by adding 1.8 N $H_2SO_4$, and optical density was measured at a wavelength of 450 and 620 nm.

**IgH sequencing of B5 specific clones**

At the end of each single B cell culture, cell pellets were resuspended in 50µl RLT Buffer (Qiagen) and stored at -80 °C. Clones whose culture had proven successful (anti-IgG and B5 ELISA OD > 0.09 for B21 cultures or IgG concentration ≥ 1 µg/mL for $MS40^{lo}$ cultures) were selected and extracted using the RNeasy Micro kit (Qiagen, B21 cultures) or the NucleoSpin96 RNA extraction kit (Macherey-Nagel, $MS40^{lo}$ cultures) according to the manufacturer's instructions. A reverse transcription step was then performed using the

SuperScript IV enzyme (ThermoFisher) in a 14 µl final volume (42 °C 10 min, 25 °C 10 min, 50 °C 60 min, 94 °C 5 min) with 4 µl of RNA and random hexamers (Thermofisher scientific). A PCR was further performed based on the protocol established by Tiller et al (Tiller et al., 2008). Briefly, 3.5 µl of cDNA was used as template and amplified in a total volume of 40 µl with a mix of forward L-VH PCR1 primers (**Table S2E**) and reverse Cγ primer and using the HotStar® Taq DNA polymerase (Qiagen) and 40 ($MS40^{lo}$ culture) or 50 cycles (B21 cultures) of PCR (94 °C 30 s, 58 °C 30 s, 72 °C 60 s). For $MS40^{lo}$ cultures, PCR products were directly sequenced with the reverse primer CHG-D1 and read on ABI PRISM 3130XL genetic analyzer (Applied Biosystems). For B21 cultures, an additional 50 cycles of PCR (94 °C 30 s, 58 °C 30 s, 72 °C 60 s) with a mix of forward L-VH PCR2 primers (**Table S2E**) was performed prior to sequencing. Sequences qualities were verified using CodonCode Aligner software (CodonCode Corporation).

**Computational analyses of VDJ sequences**

Processed FASTA sequences from cultured single-cell $V_H$ sequencing were annotated using Igblast v1.16.0 against the human IMGT reference database. Clonal cluster assignment (DefineClones.py) and germline reconstruction (CreateGermlines.py) was performed using the Immcantation/Change-O toolkit (Gupta et al., 2015) on all heavy chain V sequences. Sequences that had the same V-gene, same J-gene, including ambiguous assignments, and same CDR3 length with maximal length-normalized nucleotide hamming distance of 0.15 were considered as belonging to the same clonal group. Mutation frequencies in V genes were then calculated using the calcObservedMutations() function from the Immcantation/SHazaM v1.1.0 R package. VH repartitions were calculated using the countGenes() function from the Immcantation/alakazam v1.1.0.999 R package. Phylogenetic trees were generated using the Immcantation/IgPhyML toolkit via the dowser R package (Immcantation/suite devel docker image (Hoehn et al., 2020) and further visualized using the AncesTree GUI (Foglierini et al., 2020). Prior to mutational tree reconstruction, the first 18bp of each $V_H$ sequence was reverted to the reconstructed germline to avoid PCR2 primers-induced bias between B21 and $MS40^{lo}$ culture. CDR3 sequence logos were generated using the ggseqlogo v0.1 R package. Further clonal analyses on all productively rearranged sequences were implemented in R. Graphics were obtained using R packages ggplot2 v3.3.5 and pheatmap v1.0.12.

**Recombinant antibody production and purification**

IgH and IgL chains from clones of interest were cloned as previously described (Tiller et al., 2008). Briefly, HEK293T cells were transfected with plasmid DNA encoding paired IgH and IgL chains using Jet Prime kit (Polyplus). Recombinant antibodies were purified from supernatants using protein-G beads using manufacturer's instructions (GE Healthcare).

**Affinity measurement using biolayer interferometry (Octet)**

Biolayer interferometry assays were performed using the Octet Red96 (Sartorius). Anti-Human Fc Capture (AHC) biosensors (Sartorius Cat# 18-5060) were immersed in supernatants from single-cell MBC cultures or re-expressed monoclonal antibody at 25 °C for 500 seconds. Biosensors were equilibrated for 180 s in 1x PBS buffer with 0.1% BSA and 0.005% Tween 20 surfactant (PBS-BT) prior to measurement. Association was performed for 600s in PBS-BT with B5 protein at 100nM followed by dissociation for 900s in PBS-BT for each cycle. Biosensor regeneration was performed by alternating 30s cycles of regeneration buffer (glycine HCl, 10 mM, pH 2.0) and 30 s of PBS-BT for 3 cycles. Traces were reference sensor (unloaded sensor) and reference well (additional association cycle in the absence of B5) subtracted and curve fitting was performed using a local 1:1 binding model in the HT Data analysis software 12.2.2.26 (ForteBio).

**Single-cell RNA-seq**

The scRNA-seq dataset from 3 ITP patients (ITP1 to ITP3), 4 YD (YD1 to YD4) and 3 HD donors (HD1 to HD3) has been previously published (ArrayExpress database: E-MTAB-9955) (Crickx et al., 2021). A second dataset containing sorted naive, $IgG^+$ and $B5^+IgG^+$ memory cell had been generated in parallel from 6 HD donors (HD4 to HD9) using the same protocol. Briefly, single-cell mRNA sequencing was performed according to an adapted version of the SORT-seq protocol (Muraro et al., 2016) with primers described in van den Brink *et al*. (van den Brink et al., 2017). Cells were single-cell FACS-sorted (AriaIII) into 384-well plates containing 384 primers and Mineral oil (Sigma). After sorting, plates were snap-frozen on dry ice and stored at -80 °C. Each plate was designed to contain cells from each donor group. Of note, sorted naive/$IgG^+$ and $IgG^+B5^+$ B cells included in the dataset described in this study were prepared using a fast thawing protocol

and a subsequent apoptotic cell removal step using the Dead Cell Removal kit (Miltenyi). Sorted cells included in the previously published dataset (Crickx et al., 2021) were prepared using a slow thawing protocol at 37 °C (adapted from 10X genomics CG00039 demonstrated protocol; https://support.10xgenomics.com/single-cell-vdj/sample-prep/doc/demonstrated-protocol-fresh-frozen-human-peripheral-blood-mononuclear-cells-for-single-cell-rna-sequencing), without any additional step.

Further processing of cells, cDNA libraries generation, sequencing and reads alignment was performed at Single Cell Discoveries. For amplification, cells were heat-lysed at 65 °C followed by cDNA synthesis using the CEL-Seq2 protocol (Hashimshony et al., 2016) and robotic liquid handling platforms. After second strand cDNA synthesis, the barcoded material was pooled into libraries of 384 cells and amplified using in vitro transcription (IVT). Following amplification, the rest of the CEL-seq2 protocol was followed for preparation of the amplified cDNA library, using TruSeq small RNA primers (Illumina). The DNA library was paired-end sequenced on an Illumina Nextseq™ 500, high output, with a 2x75 bp Illumina kit. Read 1 was used for identification of the Illumina library barcode, 8 bp cell barcode and 6 bp UMI and read 2 was used to map to the reference transcriptome of Hg38 with STAR (Dobin et al., 2013). Data were demultiplexed and transcript counts were adjusted to the expected number of molecules based on counts, 4096 possible UMI's and poissonian counting statistics as described in Grün *et al*. (Grün et al., 2014). Mapping and generation of count tables was automated using the MapAndGo/starmap script (https://github.com/anna-alemany/transcriptomics/tree/master/mapandgo).

A total of 3867 MBCs, 1194 Vaccinia-specific MBCs, 1812 naives B cells and 192 GC B cells were sequenced in both datasets (**Table S3A**). Initial quality control and cell filtering was performed using the R Scater package (McCarthy et al., 2017). We removed cells where more than 50% of transcripts mapped to ERCC spike-ins, cells with less than 2000 UMIs or 500 genes detected and kept only genes that were detected in at least 2% of any given sorted cell population. Index-sorting information and parallel in vitro validation using single culture were additionally used to optimized gating strategies and remove potential sort contaminants from further analysis in the context of $IgG^+$ $B5^+$ MBCs sorts. Overall, 8326 cells and 12466 genes were left for further analysis (**Table S3A**).

Normalization, integration and clustering were then performed through the R Seurat v3 (Stuart et al., 2019) pipeline. Transcript counts were first normalized using the scTransform algorithm (Hafemeister and Satija, 2019), additionally correcting for potential bias related to the detected percentage of mitochondrial genes and selecting for the top 3000 variable features for downstream visualization and clustering analysis. After principal component analysis, sort-specific batch effects were removed using the Harmony algorithm (Korsunsky et al., 2019). The first 30 corrected principal component analysis dimensions were then used to construct a knn graph ($k$ = 20 neighbors) and perform graph-based clustering (Louvain) with a resolution parameter of 0.6 as well as compute the UMAP coordinates for each cell. Final clustering steps as presented in the manuscript were focused solely on sorted MBCs. Dotplots displaying scRNA-seq gene expression (scaled normalized counts) were generated using the Seurat Dotplot() function. Size of dots represents the percentage of cells in the cluster in which transcripts for that gene are detected. Dot color represents the average expression level (scaled normalized counts) of that gene in the population. Heatmap displaying row-scaled pseudobulk expression averaged by cluster and donor were done combining the Seurat AverageExpression() function and the ComplexHeatmap package (Gu et al., 2016).

Differential expression analyses between clusters of interest were then performed using the general linear model (GLM) likelihood ratio test implemented in the edgeR package (Chen et al., 2016) using raw transcript counts of all genes detected in at least 10% of the cells from one of the compared groups and applying a final threshold of 0.25 for log-fold-change and 0.05 for adjusted *P*-value. Regulon identification and module activity scoring in cells was done using the pySCENIC workflow (Van de Sande et al., 2020) using version 9 of cisTarget motif collection (mc9nr). SCENIC regulon identification pipeline was run independently 20 times and regulons were then curated to remove regulons not detected, or gene not associated to a given regulon, in at least 80% of run and regulons with less than 10 remaining high confidence genes.

Preranked GSEA analyses were performed using the GSEA v4.1.0 App (https://www.gsea-msigdb.org/) using HALLMARK, PID and WP pathways downloaded from the Molecular Signatures Database (MSigDB) of the Broad institute in November of 2021. For each comparison, all genes detected in at least 10% of the cells from one of the groups were

ranked based on edgeR log2FC and used as input. Summarized results from GSEA analysis are represented in **Figure 4** and **Figure S4** as dot plots using the ggplot2 package with dot size representing the Normalized Enrichment Score (NES) and dot color representing the sign of the log fold change * log10(False Discovery Rate value (FDR)). Only genesets with a NES > 1.5 and FDR < 0.01 in one of the 3 comparisons are shown. Top differentially expressed gene upregulated in cluster 0 versus cluster 1 in the leading-edge subset of each geneset are further highlighted on the right side of each plot.

All downstream analyses were performed with R v.3.5.2 on a macOS 10.13.6 (64 bit) system, using the following R packages and libraries: scater v.1.10.1, scTransform v. 0.2.1, harmony v0.99.9, Seurat v.3.1.2, reticulate v1.13, umap v0.2.4.1, edgeR v.3.32.1, ggplot2 v.3.2.1, ComplexHeatmap v2.6.2, SCENIC v 1.1.3 and AUCell v1.12.0.

**RNA and ATAC-sequencing**

$CD21^{hi}$ (upper 30%) or $CD21^{int}$ (lower 30%) $IgG^{+}$ switched memory and naive B cells were sorted from 4 independent donors (**Figure 4F**). Assay for Transposase-Accessible Chromatin with high-throughput sequencing (ATAC-seq) was performed on 50000 cells of each sorted population, according to published methods (Buenrostro et al., 2013). RNA was extracted from the remaining cells using an RNeasy Plus Microkit (Qiagen) and sent for library preparation and sequencing by Integragen (Evry, France). Libraries were prepared using the NEBNext Ultra II Directional RNA Library Prep Kit for Illumina protocol according to supplier recommendations and sequenced (2 x 100 bp, paired-ends; Illumina NovaSeq$^{TM}$6000) at IntegraGen (Evry, France).

RNA-seq reads were aligned against the hg38 human genome using STAR (Dobin et al., 2013), keeping only reads with a single alignment. Raw counts for each sample were obtained using featureCounts.py from the SubRead package (Liao et al., 2013). Differential expression of filtered genes (HTSfilter, 11104 genes) was analyzed using DESeq2 v1.28.1 (Love et al., 2014) in R (version 4.0.0). Differentially expressed genes were selected with an adjusted value of $P < 0.05$ and a fold-change > 2 after Wald's test and Benjamini-Hochberg correction. Principal component analysis (PCA) was performed on DESeq2-normalized read counts for the fold-change–filtered genes. Preranked GSEA analyses were performed as described above using all genes ranked based on DESeq2 residuals as input.

Only genesets with a NES > 1.5 and FDR < 0.05 in one of the comparisons are reported in **Figure S4** and **Figure 5**.

ATAC-seq reads were aligned against the hg38 human genome, using Bowtie1 (Langmead et al., 2009). Open regions were determined with Model-Based Analysis of ChIP-Seq2 (MACS2) (Feng et al., 2012) and filtered with a value of $q < 0.001$. Read counts were determined by using featureCounts.py from the SubRead package (Liao et al., 2013), and differentially opened (DO) regions were identified with DESeq2 (Love et al., 2014) with a fold-change in accessibility > 2 and an adjusted value of $P < 0.05$ after Wald's test and Benjamini- Hochberg correction. Generated libraries from one of the donors did not reach our quality control cut-offs and all ATAC-seq data from that donor were excluded from further analysis.

Graphical representations, data integration, and statistical analyses were generated with R.

**Seahorse metabolic experiments**

Human naive and $IgG^+$ switched MBCs from 5 HD donors were sorted, washed with the appropriate buffer according to the experiment and seeded at a density of 200,000 to 300,000 cells per well in a XFe96 cell culture microplate. Cells were balanced for 1 h in relevant media prior to measurements. Each test was conducted according to the manufacturer's recommendation and ECAR and OCR measured using a XF96 extracellular flux analyzer (Seahorse Bioscience, Agilent Technologies). Briefly, for mitochondrial respiration, unbuffered XF assay media (Agilent Technologies) supplemented with 2 mM glutamine, 10 mM glucose and 1 mM sodium pyruvate was used. After measurement of basal OCR, Oligomycin (ATP synthase inhibitor, 1 µM), FCCP (uncoupling agent measuring the maximal respiration capacity; 1 µM) and Antimycin A (ETC inhibitor; 1 µM) were sequentially injected. For glycolytic function, unbuffered XF assay media supplemented with 2 mM glutamine was used. After measurement of basal ECAR, glucose (10 mM), oligomycin (1 µM), and 2-deoxyglucose (2-DG, glycolytic inhibitor; 500 mM) were sequentially injected. For glutamine oxidation, unbuffered XF assay media supplemented with 10 mM glucose and 1 mM sodium pyruvate was used. After measurement of basal OCR, glutamine (2 mM) and BPTES (3 µM) were sequentially injected. For Glycolytic rate assay profile: Seahorse XF Base Medium without phenol red

(Agilent technologies) with 2 mM glutamine, 10 mM glucose, 1 mM sodium pyruvate and 5.0 mM HEPES. After measurement of basal ECAR and OCR, rotenone (1 µM) and 2-DG (500 mM) were sequentially injected, and proton efflux rate was assessed.

For fatty acid oxidation (FAO) tests, cells were plated in FAO assay media (110 mM NaCl, 4.7 mM KCl, 1.25 mM CaCl2, 2 mM MgSO4, 1.2 mM NaH2PO4, 2.5 mM Glucose, 0.5 mM Carnitine, and 5 mM HEPES) supplemented either with BSA (100 µM) or BSA + etomoxir (200 µM). After measurement of basal OCR, oligomycin (1 µM), FCCP (1 µM), antimycin A (1 µM) were sequentially injected.

**Isotopic profiling by LC-HRMS**

Human naive and $IgG^+$ switched memory from 3 HD donors were sorted, washed with glucose-free or glutamine-free RPMI-1640 and seeded at a density of 1,000,000 cells/mL in FACS tubes in glucose-free RPMI-1640 supplemented with 11mM $^{13}C_6$-D-Glucose (Sigma, Cat# 389374) and 2% FCS or glutamine-free RPMI-1640 supplemented with 2 mM $^{13}C_5$-L-Glutamine (Sigma, Cat# 605166) and 2% FCS respectively. 1 mL (1,000,000 cells) of each cell suspension was harvested at 0 hr, 1 hr and 6 hrs and cells were quenched by rapid filtration on a 0.2 µM polyamide membrane filter (Sartolon, Cat# 25007-47-N). The filter was snap frozen in liquid nitrogen at −196 °C and stored at -80 °C until extraction.

Subsequent extraction and analysis of metabolites was performed on the MetaToul metabolic platform (INSA Toulouse, FRANCE). Extraction was done with a solvent mixture of ACN/Methanol/$H_2O$ (2:2:1) at −20 °C. Samples were then evaporated and resuspended in 120 µL of ultrapure $H_2O$ before analysis. The analyses of metabolites were carried out on liquid anion exchange chromatography DionexTM ICS-5000+ Reagent-FreeTM HPICTM (Thermo Fisher ScientificTM, Sunnyvale, CA, USA) system coupled to QExactiveTM Plus high-resolution mass spectrometer (Thermo Fisher ScientificTM, Waltham, MA).

Liquid anion exchange chromatography was performed with the Thermo Scientific Dionex ICS-5000+ Reagent-Free HPIC system (Thermo Fisher Scientific) equipped with an eluent generator system (ICS-5000+EG, Dionex) for automatic base generation (KOH). Analytes were separated within 50 min, using a linear KOH gradient elution applied to an IonPac

AS11- HC column (250 x 2 mm, Dionex) equipped with an AG11-HC guard column (50 x 2 mm, Dionex) at a flow rate of 0.38 ml/min. The gradient was as follows: equilibration with 7 mM KOH during 1.0 min; then KOH ramp from 7 to 15 mM, 1–9.5 min; constant concentration 10.5 min; ramp to 45 mM in 10 min; ramp to 70 mM in 3 min; ramp to 100 mM in 0.1 min; constant concentration 8.9 min; drop to 7 mM in 0.5 min; and equilibration at 7 mM KOH for 7.5 min. The column and autosampler temperatures were thermostated at 25 °C and 4 °C, respectively. The injected sample volume was 15 µl. Measures were performed in triplicates from separate cultures.

MS analyses were performed in negative FTMS mode at a resolution of 70 000 (at 400 m/z) in full-scan mode, with the following source parameters: the capillary temperature was 325 °C, the source heater temperature, 350 °C, the sheath gas flow rate, 50 a.u. (arbitrary unit), the auxiliary gas flow rate, 5 a.u., the S-Lens RF level, 50 %, and the source voltage, 2.75 kV. Metabolites were determined by extracting the exact mass with a tolerance of 5 ppm.

13C-profiler-emzed software was used for data processing. Isocor 2.0 was used for correction of natural abundance of occurring isotopes taking into account correction of the isotopic tracer for a 99% theoretical 13C purity in substrates.

**TeloFISH**

25000 naive, $IgG^+$ switched memory or marginal zone B cells were directly sorted in individual wells of a Poly-L-Lysine coated 8 wells HTC slide (Thermo Scientific, Cat# 30-8H-RED-CE24) in an initial 1x PBS drop of 5 µL. 25000 Muntjac fibroblasts (Benyelles et al., 2019), used as reference, were further sorted on to each well and cells were left to sediment for 30 to 45 min at RT before fixation in Electron Microscopy grade 4% formaldehyde solution (Electron Microscopy Sciences, Cat#15714). For donor from whom $B5^+$ $IgG^+$ cells were also analyzed ($n$ = 6), all B cell population were sorted after an initial enrichment step on a BD FACSAria III cell sorter ($IgG^+$ versus $IgG^-CD3^-CD14^-CD16^-$, yield mode) and $B5^+IgG^+$ cells were sorted in a 1x PBS drop of 10µL alongside 200 Muntjac cells and left to sediment 5 to 10 min prior to fixation. A control well with 200 sorted $B5^-IgG^+$ cells was always performed. Cells were then washed three times in 1x PBS and the slides were dehydrated and air-dried. A hybridization mixture containing 70%

formamide, 20 mM Tris, 100 nM TelC-Cy3 PNA probe (Panagene, Cat#F1002), and 1% blocking reagent (Roche, Cat# 11096176001) was added. DNA was denatured by heat at 82 °C for 5min. After hybridization at RT for 1.5 hrs, slides were washed successively with 70% formamide (2 x 15 min) and with 0.05 M Tris, 0.15 M NaCl, and 0.05% Tween-20 (3 x 5 min). Slides were then dehydrated in ethanol, air-dried, and mounted using DAPI-containing VECTASHIELD Antifade Mounting Medium (Eurobio, Cat# H-1200).

Imaging was performed on a ZEISS Apotome 2 microscope using a 63x objective. All image analyses were performed in Icy (icy.bioimageanalysis.org) using Spot detector algorithm (Olivo-Marin, 2002). Measured intensities are expressed as a ratio over the mean intensity detected for telomeres in spike-in Muntjac cells in the same image (at least 5 per image).

**Telomeric Restriction Fragment.**

Naive, $IgG^+$ switched memory and marginal zone B cells were sorted and stored as dry pellets at -80 °C. DNA was extracted using the AllPrep RNA/DNA Micro Kit (Qiagen, Cat# 80284). DNA (1 μg) was digested with HinfI and RsaI enzymes, resolved by a 0.7% agarose gel, and transferred to a nylon membrane. Hybridization was performed at 42 °C using EasyHyb solution (Roche) with γ-32P-labeled (TTAGGG)4 probe. After washes, membranes were exposed over a PhosphorImager (AGFA). PhosphorImager exposures of telomere-probed Southern blots were analyzed with the ImageJ program. The digitalized signal data were then transferred to Microsoft Excel and served as the basis for calculating mean TRF length using the formula $L = \Sigma(ODi)/\Sigma(ODi/Li)$, where OD is the intensity of the hybridization signal and L is the length, in Kb, at the gel point i.

**Illustration tool**

All figures were assembled using Adobe Illustrator (CS6). The graphical abstract was created with Biorender.com.

**Quantification and Statistical Analysis**

Wilcoxon matched-pairs signed rank tests, Kruskal-Wallis tests, non-parametric Friedman tests, repeated measure one-way or two-way ANOVA tests were used to compare continuous variables as appropriate (indicated in Figures). Benjamini, Krieger and

Yekutieli FDR correction was used for all multiple comparisons. A *P*-value ≤ 0.05 was considered statistically significant. In all figure panels, only significant *P*-values are reported, except for Figures 7C. Statistical analyses were all performed using GraphPad Prism 9.0 (La Jolla, CA, USA).

**Additional resources**.

**Excel table titles**

Table S1. Human donors' information, experimental inclusion and splenic B cell profiling, related to all Figures and supplementary Figures.

Table S2. VDJ sequencing, index sorting and affinity measurement. Related to Figures 2 and 3 and Figures S2.

Table S3. single cell RNA sequencing analysis. Related to Figures 3 and 4 and Figure S4.

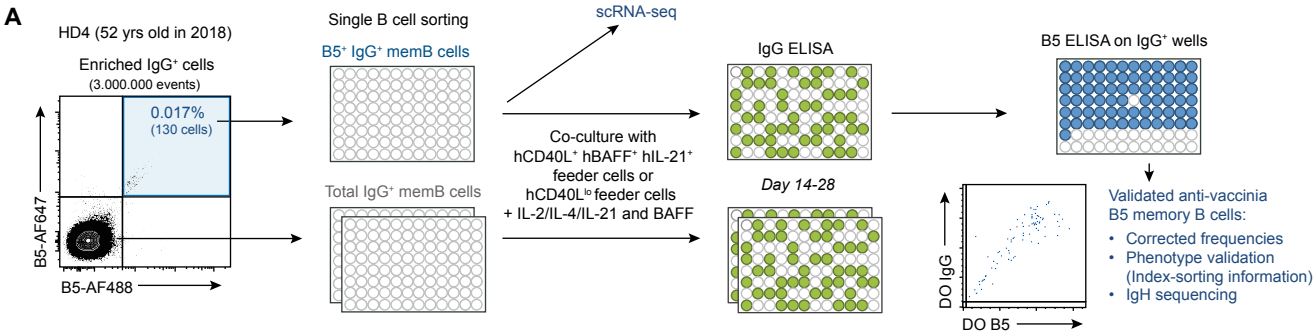
A
HD4 (52 yrs old in 2018)
Enriched IgG+ cells
(3.000.000 events)
0.017%
(130 cells)
B5-AF647
B5-AF488
Single B cell sorting
B5+ IgG+ memB cells
Total IgG+ memB cells
scRNA-seq
Co-culture with
hCD40L+ hBAFF+ hIL-21+
feeder cells or
hCD40Llo feeder cells
+ IL-2/IL-4/IL-21 and BAFF
IgG ELISA
Day 14-28
B5 ELISA on IgG+ wells
DO IgG
DO B5
Validated anti-vaccinia
B5 memory B cells:
• Corrected frequencies
• Phenotype validation
(Index-sorting information)
• IgH sequencing

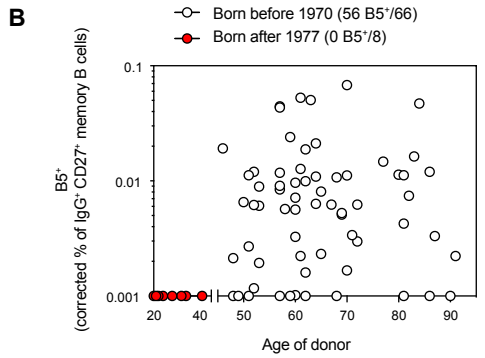
B
Born before 1970 (56 B5+/66)
Born after 1977 (0 B5+/8)
B5+
(corrected % of IgG+ CD27+ memory B cells)
0.1
0.01
0.001
20
40
50
60
70
80
90
Age of donor

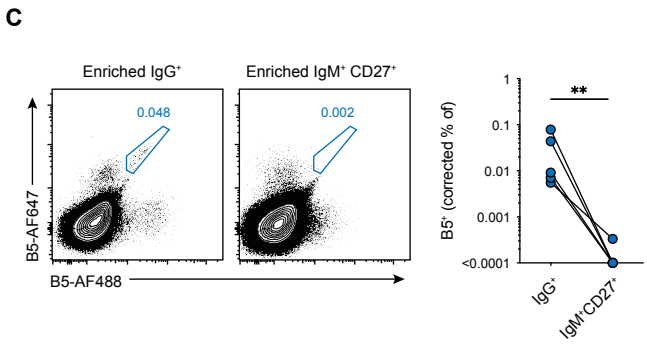
C
Enriched IgG+
Enriched IgM+ CD27+
0.048
0.002
B5-AF647
B5-AF488
B5+ (corrected % of)
1
0.1
0.01
0.001
<0.0001
**
IgG+
IgM+CD27+

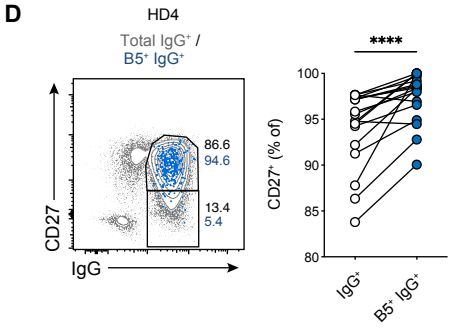
D
HD4
Total IgG+ /
B5+ IgG+
86.6
94.6
13.4
5.4
CD27
IgG
****
CD27+ (% of)
100
95
90
85
80
IgG+
B5+ IgG+

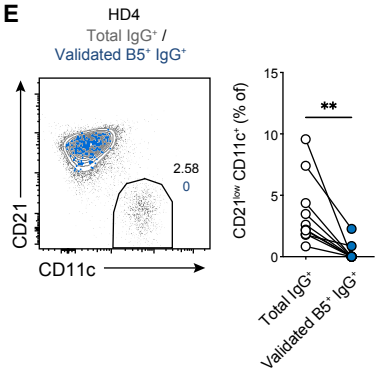
E
HD4
Total IgG+ /
Validated B5+ IgG+
2.58
0
CD21
CD11c
CD21low CD11c+ (% of)
15
10
5
0
**
Total IgG+
Validated B5+ IgG+

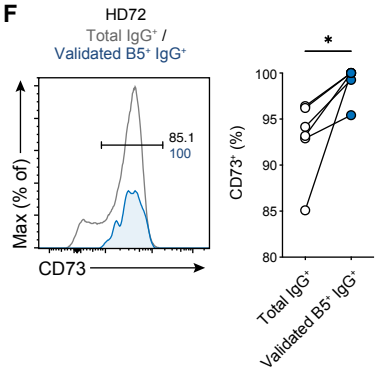
F
HD72
Total IgG+ /
Validated B5+ IgG+
85.1
100
Max (% of)
CD73
CD73+ (%)
100
95
90
85
80
*
Total IgG+
Validated B5+ IgG+

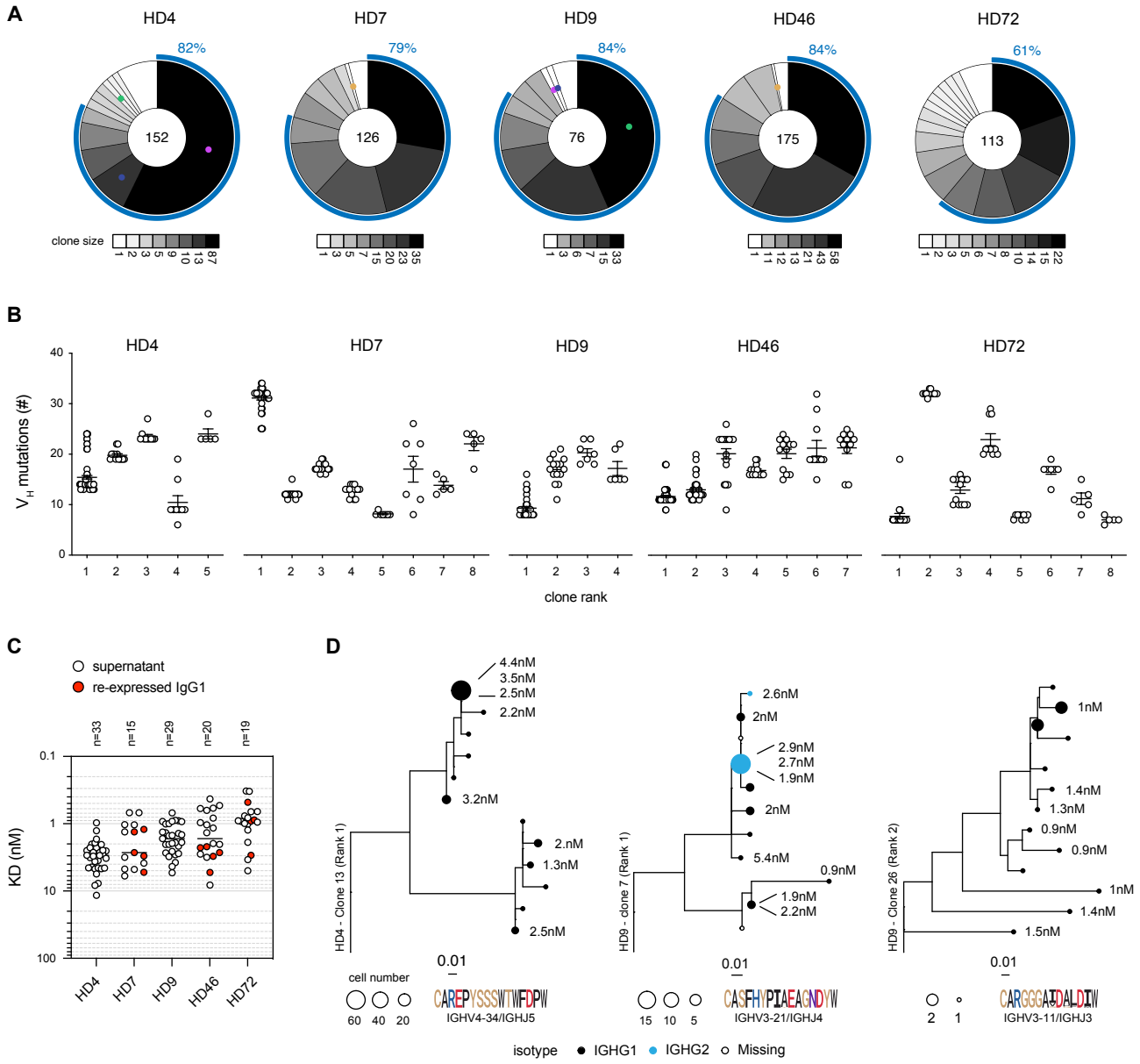
A
HD4
HD7
HD9
HD46
HD72
82%
79%
84%
84%
61%
152
126
76
175
113
clone size
B
HD4
HD7
HD9
HD46
HD72
$V_H$ mutations (#)
clone rank
C
supernatant
re-expressed IgG1
n=33
n=15
n=29
n=20
n=19
KD (nM)
HD4
HD7
HD9
HD46
HD72
D
HD4 - Clone 13 (Rank 1)
4.4nM
3.5nM
2.5nM
2.2nM
3.2nM
2.nM
1.3nM
2.5nM
HD9 - clone 7 (Rank 1)
2.6nM
2nM
2.9nM
2.7nM
1.9nM
2nM
5.4nM
0.9nM
1.9nM
2.2nM
HD9 - Clone 26 (Rank 2)
1nM
1.4nM
1.3nM
0.9nM
0.9nM
1nM
1.4nM
1.5nM
cell number
0.01
IGHV4-34/IGHJ5
IGHV3-21/IGHJ4
IGHV3-11/IGHJ3
isotype
IGHG1
IGHG2
Missing
E
HD4 - Clone 13 (Rank 1): IGHV4-34/IGHJ5
FR1
CDR1
FR2
CDR2
FR3
CDR3
FR4
Germline

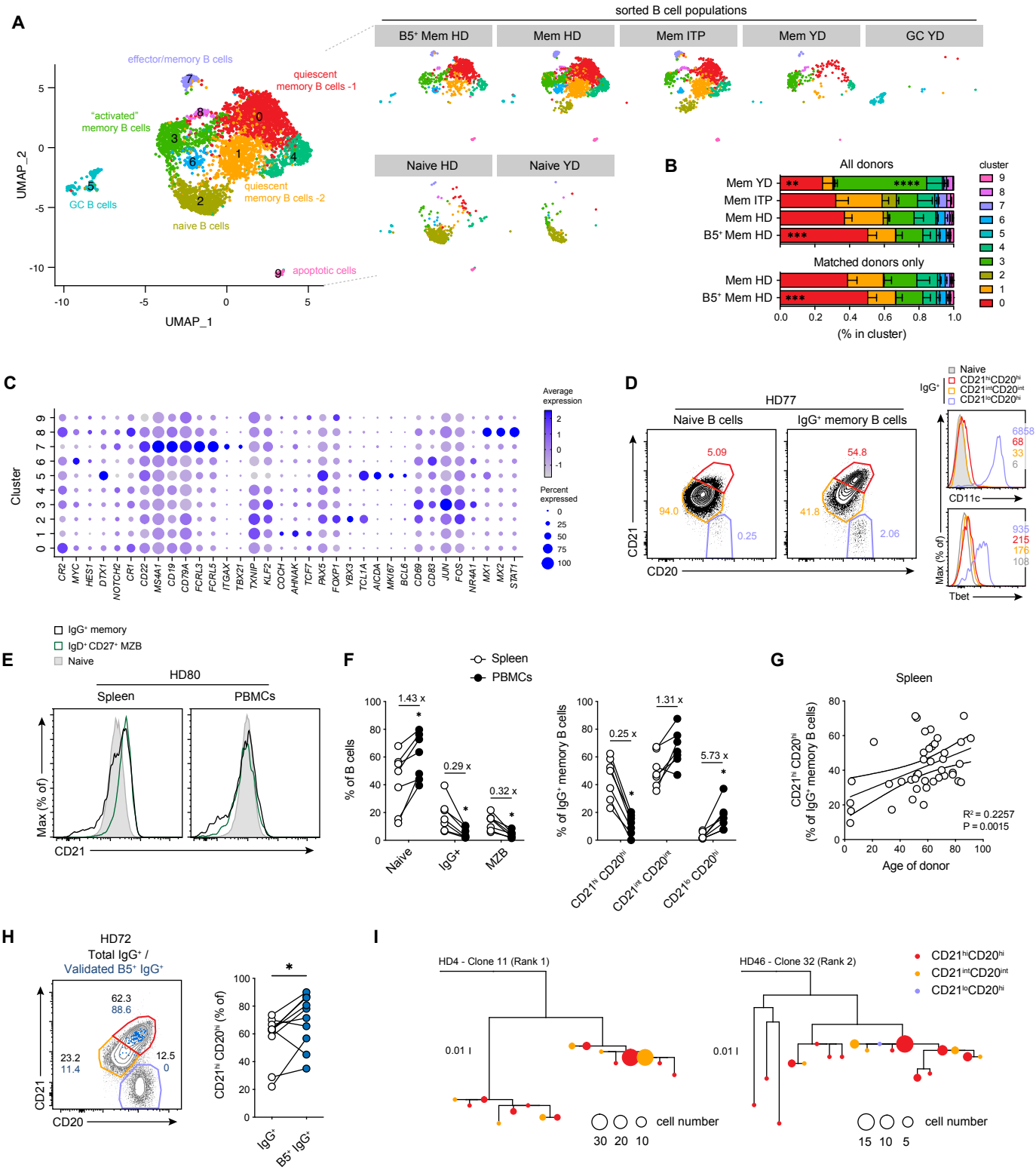
A
sorted B cell populations
B5⁺ Mem HD
Mem HD
Mem ITP
Mem YD
GC YD
Naive HD
Naive YD
effector/memory B cells
quiescent memory B cells -1
"activated" memory B cells
quiescent memory B cells -2
GC B cells
naive B cells
apoptotic cells
UMAP_1
UMAP_2
B
All donors
Matched donors only
Mem YD
Mem ITP
Mem HD
B5⁺ Mem HD
(% in cluster)
cluster
C
Cluster
Average expression
Percent expressed
CR2 MYC HES1 DTX1 NOTCH2 CR1 CD22 MS4A1 CD19 CD79A FCRL3 FCRL5 ITGAX TBX21 TXNIP KLF2 COCH AHNAK TCF7 PAX5 FOXP1 YBX3 TCL1A AICDA MKI67 BCL6 CD69 CD83 JUN FOS NR4A1 MX1 MX2 STAT1
D
HD77
Naive B cells
IgG⁺ memory B cells
CD21
CD20
IgG⁺
Naive
CD21ʰⁱCD20ʰⁱ
CD21ⁱⁿᵗCD20ⁱⁿᵗ
CD21ˡᵒCD20ʰⁱ
CD11c
Tbet
Max (% of)
E
IgG⁺ memory
IgD⁺CD27⁺ MZB
Naive
HD80
Spleen
PBMCs
Max (% of)
CD21
F
Spleen
PBMCs
% of B cells
% of IgG⁺ memory B cells
Naive
IgG+
MZB
CD21ʰⁱ CD20ʰⁱ
CD21ⁱⁿᵗ CD20ⁱⁿᵗ
CD21ˡᵒ CD20ʰⁱ
G
Spleen
CD21ʰⁱ CD20ʰⁱ (% of IgG⁺ memory B cells)
Age of donor
R² = 0.2257
P = 0.0015
H
HD72
Total IgG⁺ /
Validated B5⁺ IgG⁺
CD21
CD20
CD21ʰⁱ CD20ʰⁱ (% of)
IgG⁺
B5⁺ IgG⁺
I
HD4 - Clone 11 (Rank 1)
HD46 - Clone 32 (Rank 2)
0.01
cell number
30 20 10
15 10 5
CD21ʰⁱCD20ʰⁱ
CD21ⁱⁿᵗCD20ⁱⁿᵗ
CD21ˡᵒCD20ʰⁱ

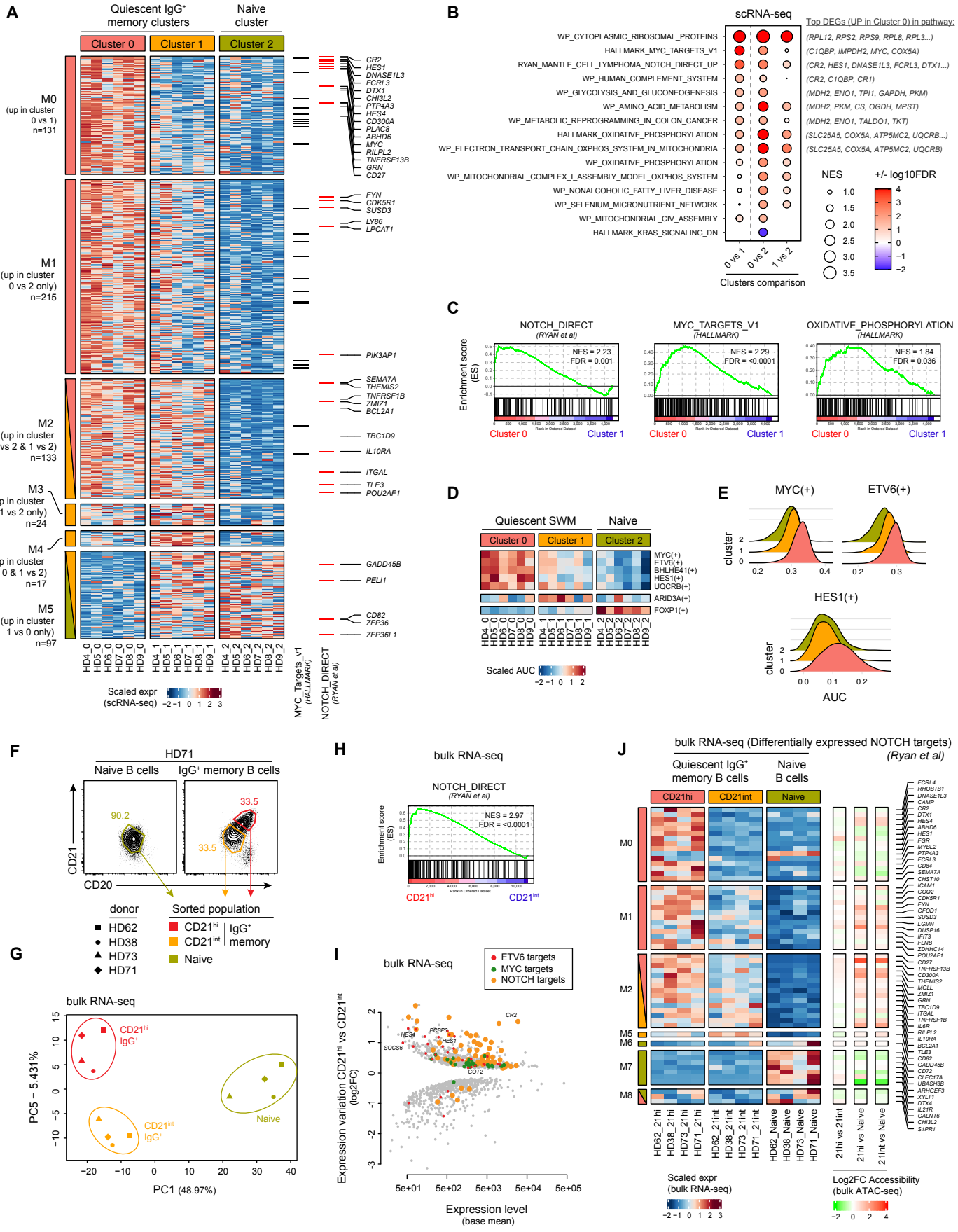
A
Quiescent IgG+ memory clusters
Naive cluster
Cluster 0
Cluster 1
Cluster 2
M0 (up in cluster 0 vs 1) n=131
M1 (up in cluster 0 vs 2 only) n=215
M2 (up in cluster 0 vs 2 & 1 vs 2) n=133
M3 (up in cluster 1 vs 2 only) n=24
M4 (up in cluster 1 vs 0 & 1 vs 2) n=17
M5 (up in cluster 1 vs 0 only) n=97
CR2
HES1
DNASE1L3
FCRL3
DTX1
CHI3L2
PTP4A3
HES4
CD300A
PLAC8
ABHD6
MYC
RILPL2
TNFRSF13B
GRN
CD27
FYN
CDK5R1
SUSD3
LY86
LPCAT1
PIK3AP1
SEMA7A
THEMIS2
TNFRSF1B
ZMIZ1
BCL2A1
TBC1D9
IL10RA
ITGAL
TLE3
POU2AF1
GADD45B
PELI1
CD82
ZFP36
ZFP36L1
Scaled expr (scRNA-seq)
MYC_Targets_v1 (HALLMARK)
NOTCH_DIRECT (RYAN et al)
B
scRNA-seq
Top DEGs (UP in Cluster 0) in pathway:
WP_CYTOPLASMIC_RIBOSOMAL_PROTEINS (RPL12, RPS2, RPS9, RPL8, RPL3...)
HALLMARK_MYC_TARGETS_V1 (C1QBP, IMPDH2, MYC, COX5A)
RYAN_MANTLE_CELL_LYMPHOMA_NOTCH_DIRECT_UP (CR2, HES1, DNASE1L3, FCRL3, DTX1...)
WP_HUMAN_COMPLEMENT_SYSTEM (CR2, C1QBP, CR1)
WP_GLYCOLYSIS_AND_GLUCONEOGENESIS (MDH2, ENO1, TPI1, GAPDH, PKM)
WP_AMINO_ACID_METABOLISM (MDH2, PKM, CS, OGDH, MPST)
WP_METABOLIC_REPROGRAMMING_IN_COLON_CANCER (MDH2, ENO1, TALDO1, TKT)
HALLMARK_OXIDATIVE_PHOSPHORYLATION (SLC25A5, COX5A, ATP5MC2, UQCRB...)
WP_ELECTRON_TRANSPORT_CHAIN_OXPHOS_SYSTEM_IN_MITOCHONDRIA (SLC25A5, COX5A, ATP5MC2, UQCRB)
WP_OXIDATIVE_PHOSPHORYLATION
WP_MITOCHONDRIAL_COMPLEX_I_ASSEMBLY_MODEL_OXPHOS_SYSTEM
WP_NONALCOHOLIC_FATTY_LIVER_DISEASE
WP_SELENIUM_MICRONUTRIENT_NETWORK
WP_MITOCHONDRIAL_CIV_ASSEMBLY
HALLMARK_KRAS_SIGNALING_DN
0 vs 1
0 vs 2
1 vs 2
Clusters comparison
NES
+/- log10FDR
C
NOTCH_DIRECT (RYAN et al)
NES = 2.23
FDR = 0.001
MYC_TARGETS_V1 (HALLMARK)
NES = 2.29
FDR = <0.0001
OXIDATIVE_PHOSPHORYLATION (HALLMARK)
NES = 1.84
FDR = 0.036
Enrichment score (ES)
Cluster 0
Cluster 1
D
Quiescent SWM
Naive
MYC(+)
ETV6(+)
BHLHE41(+)
HES1(+)
UQCRB(+)
ARID3A(+)
FOXP1(+)
Scaled AUC
E
MYC(+)
ETV6(+)
HES1(+)
cluster
AUC
F
HD71
Naive B cells
IgG+ memory B cells
90.2
33.5
33.5
CD21
CD20
donor
HD62
HD38
HD73
HD71
Sorted population
CD21hi IgG+ memory
CD21int IgG+ memory
Naive
G
bulk RNA-seq
CD21hi IgG+
CD21int IgG+
Naive
PC5 – 5.431%
PC1 (48.97%)
H
bulk RNA-seq
NOTCH_DIRECT (RYAN et al)
NES = 2.97
FDR = <0.0001
Enrichment score (ES)
CD21hi
CD21int
I
bulk RNA-seq
ETV6 targets
MYC targets
NOTCH targets
CR2
HES4
PCBP3
HES1
SOCS6
GOT2
Expression variation CD21hi vs CD21int (log2FC)
Expression level (base mean)
J
bulk RNA-seq (Differentially expressed NOTCH targets)
(Ryan et al)
Quiescent IgG+ memory B cells
Naive B cells
CD21hi
CD21int
Naive
M0
M1
M2
M5
M6
M7
M8
HD62_21hi
HD38_21hi
HD73_21hi
HD71_21hi
HD62_21int
HD38_21int
HD73_21int
HD71_21int
HD62_Naive
HD38_Naive
HD73_Naive
HD71_Naive
21hi vs 21int
21hi vs Naive
21int vs Naive
Scaled expr (bulk RNA-seq)
Log2FC Accessibility (bulk ATAC-seq)

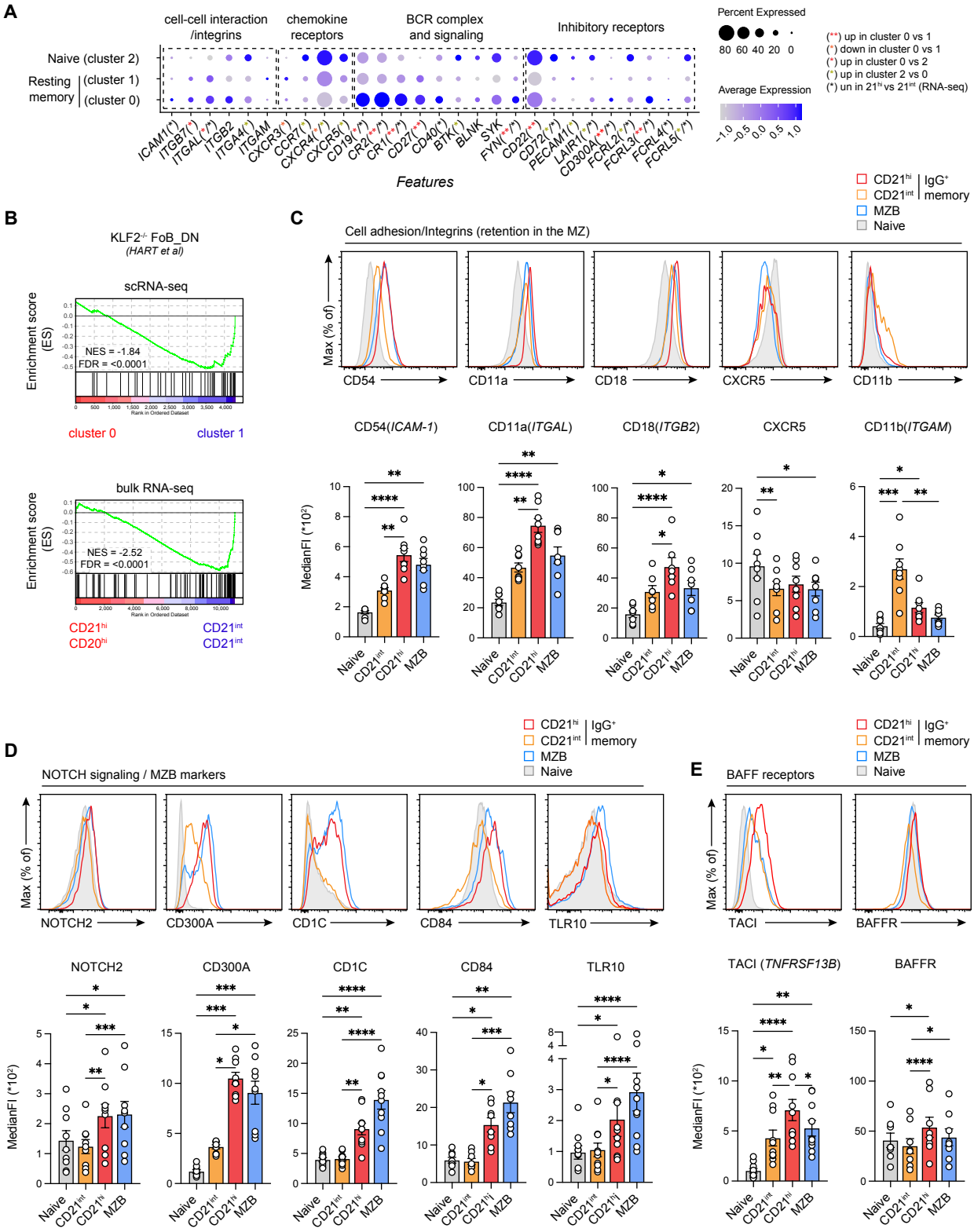
A
cell-cell interaction /integrins
chemokine receptors
BCR complex and signaling
Inhibitory receptors
Naive (cluster 2)
Resting memory (cluster 1)
(cluster 0)
ICAM1(*) ITGB7(*) ITGAL(**/*) ITGB2 ITGA4(*) ITGAM CXCR3(*) CCR7(*/*) CXCR4(*/*) CXCR5(*) CD19(*/*) CR2(**/*) CR1(**/*) CD27(**) CD40(*) BTK(*) BLNK SYK FYN(**/*) CD22(**) CD72(*/*) PECAM1(*/*) LAIR1(*/*) CD300A(**/*) FCRL2(*/*) FCRL3(**/*) FCRL4(*) FCRL5(*/*)
Features
Percent Expressed
80 60 40 20 0
Average Expression
-1.0 -0.5 0.0 0.5 1.0
(**) up in cluster 0 vs 1
(*) down in cluster 0 vs 1
(*) up in cluster 0 vs 2
(*) up in cluster 2 vs 0
(*) un in 21hi vs 21int (RNA-seq)
B
KLF2-/- FoB_DN (HART et al)
scRNA-seq
Enrichment score (ES)
NES = -1.84
FDR = <0.0001
cluster 0
cluster 1
bulk RNA-seq
NES = -2.52
FDR = <0.0001
CD21hi CD20hi
CD21int CD21int
C
CD21hi IgG+ memory
CD21int
MZB
Naive
Cell adhesion/Integrins (retention in the MZ)
Max (% of)
CD54
CD11a
CD18
CXCR5
CD11b
CD54(ICAM-1)
CD11a(ITGAL)
CD18(ITGB2)
CXCR5
CD11b(ITGAM)
MedianFI (*10²)
Naive CD21int CD21hi MZB
D
NOTCH signaling / MZB markers
NOTCH2
CD300A
CD1C
CD84
TLR10
E
BAFF receptors
TACI
BAFFR
TACI (TNFRSF13B)
BAFFR

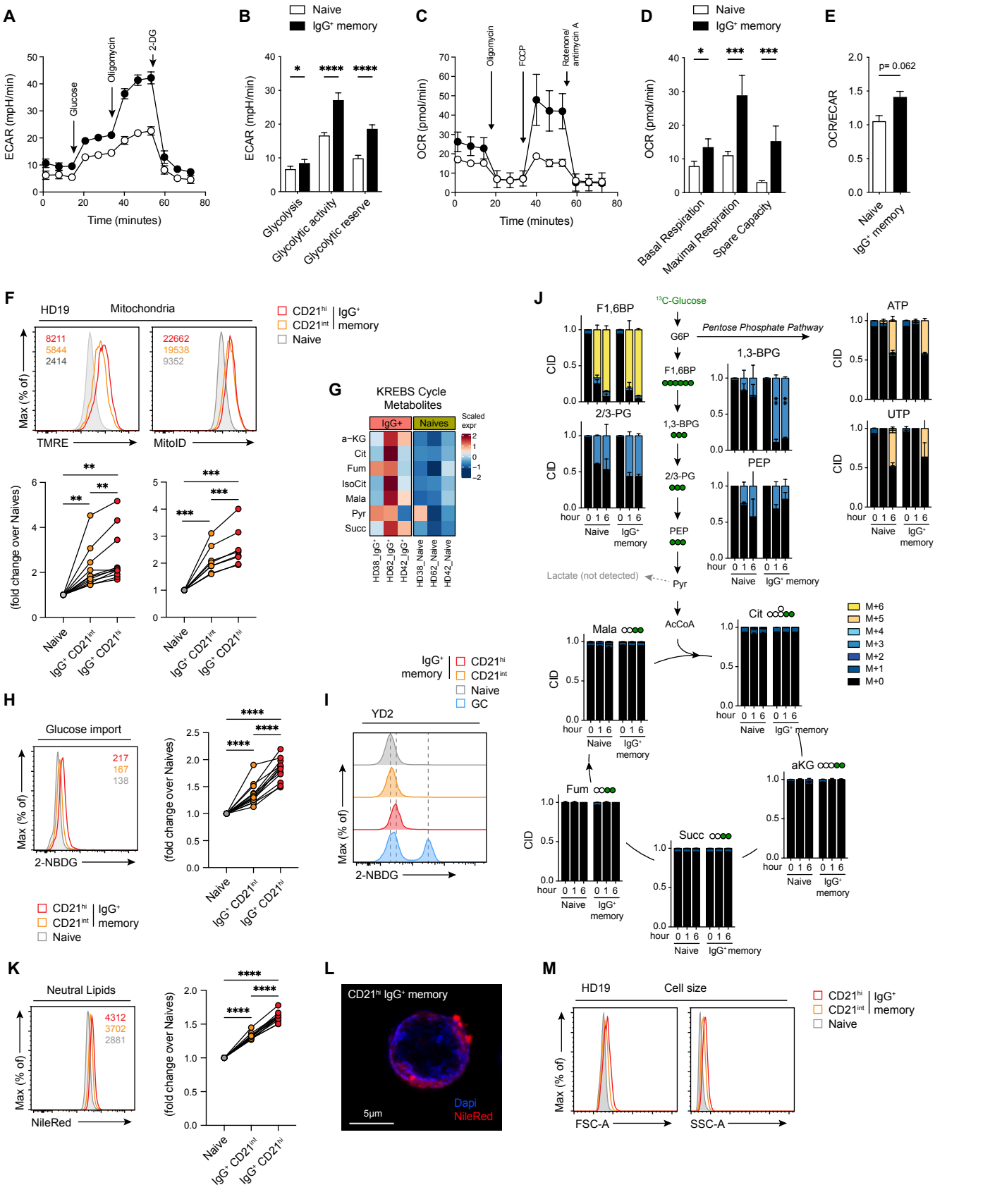
A
ECAR (mpH/min)
Glucose
Oligomycin
2-DG
Time (minutes)
B
Naive
IgG+ memory
ECAR (mpH/min)
Glycolysis
Glycolytic activity
Glycolytic reserve
C
OCR (pmol/min)
Oligomycin
FCCP
Rotenone/ antimycin A
Time (minutes)
D
Naive
IgG+ memory
OCR (pmol/min)
Basal Respiration
Maximal Respiration
Spare Capacity
E
OCR/ECAR
p= 0.062
Naive
IgG+ memory
F
HD19
Mitochondria
CD21hi IgG+ memory
CD21int IgG+ memory
Naive
Max (% of)
8211
5844
2414
TMRE
22662
19538
9352
MitoID
(fold change over Naives)
Naive
IgG+ CD21int
IgG+ CD21hi
G
KREBS Cycle Metabolites
IgG+
Naives
Scaled expr
a-KG
Cit
Fum
IsoCit
Mala
Pyr
Succ
HD38_IgG+
HD62_IgG+
HD42_IgG+
HD38_Naive
HD62_Naive
HD42_Naive
J
13C-Glucose
Pentose Phosphate Pathway
G6P
F1,6BP
1,3-BPG
2/3-PG
PEP
Pyr
Lactate (not detected)
AcCoA
Mala
Cit
Fum
Succ
aKG
ATP
UTP
CID
hour 0 1 6
Naive
IgG+ memory
M+6
M+5
M+4
M+3
M+2
M+1
M+0
H
Glucose import
217
167
138
2-NBDG
Max (% of)
(fold change over Naives)
CD21hi IgG+ memory
CD21int IgG+ memory
Naive
I
YD2
Max (% of)
2-NBDG
IgG+ memory
CD21hi
CD21int
Naive
GC
K
Neutral Lipids
4312
3702
2881
NileRed
Max (% of)
(fold change over Naives)
L
CD21hi IgG+ memory
5µm
Dapi
NileRed
M
HD19
Cell size
CD21hi IgG+ memory
CD21int IgG+ memory
Naive
Max (% of)
FSC-A
SSC-A

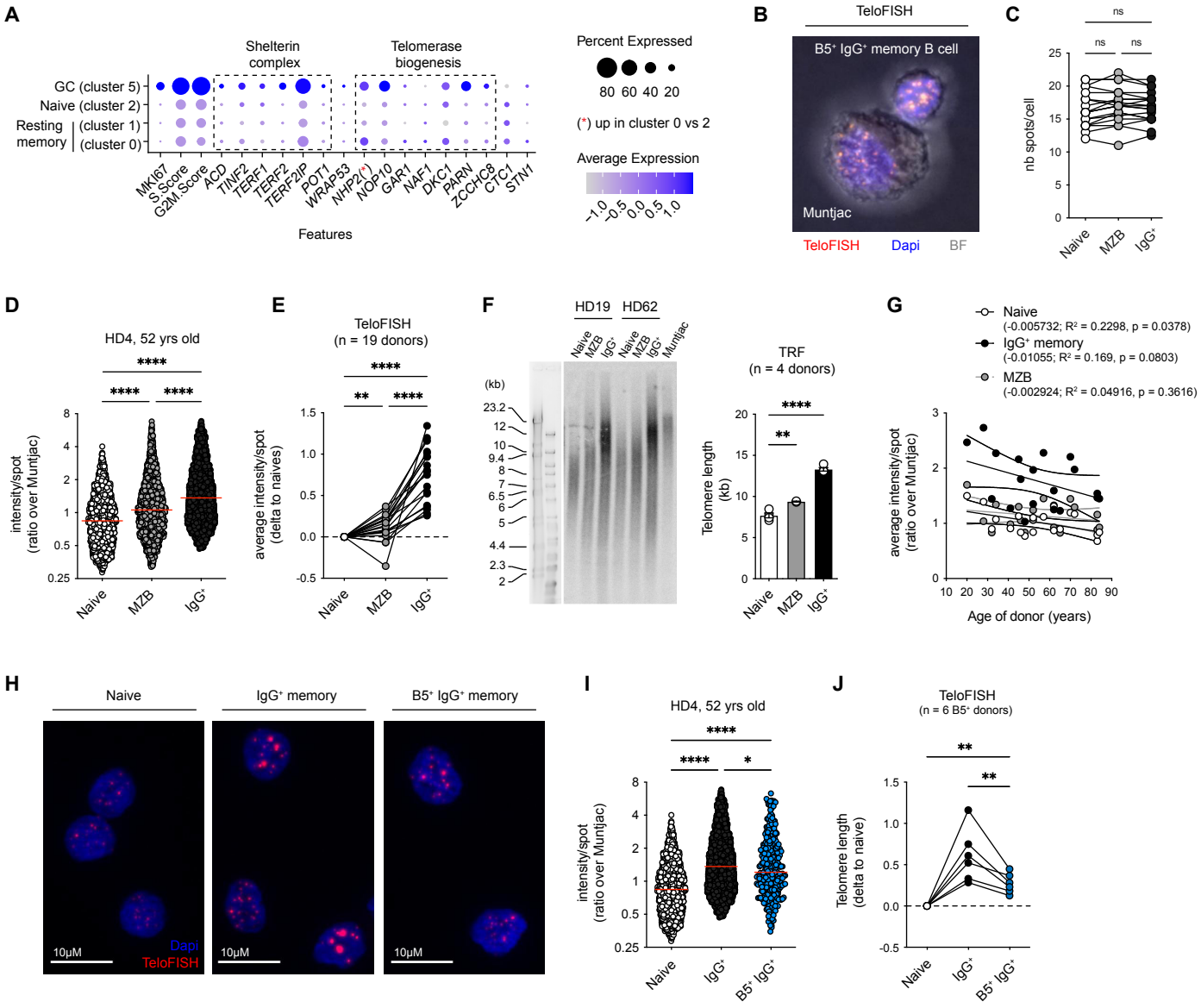
A
Shelterin complex
Telomerase biogenesis
GC (cluster 5)
Naive (cluster 2)
Resting memory
(cluster 1)
(cluster 0)
MKI67
S.Score
G2M.Score
ACD
TINF2
TERF1
TERF2
TERF2IP
POT1
WRAP53
NHP2(*)
NOP10
GAR1
NAF1
DKC1
PARN
ZCCHC8
CTC1
STN1
Features
Percent Expressed
80 60 40 20
(*) up in cluster 0 vs 2
Average Expression
−1.0 −0.5 0.0 0.5 1.0
B
TeloFISH
B5⁺ IgG⁺ memory B cell
Muntjac
TeloFISH
Dapi
BF
C
ns
ns
ns
nb spots/cell
Naive
MZB
IgG⁺
D
HD4, 52 yrs old
****
****
****
intensity/spot (ratio over Muntjac)
Naive
MZB
IgG⁺
E
TeloFISH (n = 19 donors)
****
**
****
average intensity/spot (delta to naives)
Naive
MZB
IgG⁺
F
HD19
HD62
Naive
MZB
IgG⁺
Naive
MZB
IgG⁺
Muntjac
(kb)
23.2
12
10
9.4
8
7
6.5
6
5
4.4
2.3
2
TRF (n = 4 donors)
****
**
Telomere length (kb)
Naive
MZB
IgG⁺
G
Naive (-0.005732; R² = 0.2298, p = 0.0378)
IgG⁺ memory (-0.01055; R² = 0.169, p = 0.0803)
MZB (-0.002924; R² = 0.04916, p = 0.3616)
average intensity/spot (ratio over Muntjac)
Age of donor (years)
H
Naive
IgG⁺ memory
B5⁺ IgG⁺ memory
10µM
Dapi
TeloFISH
I
HD4, 52 yrs old
****
****
*
intensity/spot (ratio over Muntjac)
Naive
IgG⁺
B5⁺ IgG⁺
J
TeloFISH (n = 6 B5⁺ donors)
**
**
Telomere length (delta to naive)
Naive
IgG⁺
B5⁺ IgG⁺